Microporous and Mesoporous Materials 267 (2018) 274–292

Contents lists available at ScienceDirect

Microporous and Mesoporous Materials

journal homepage: www.elsevier.com/locate/micromeso

Highlighting the origins and consequences of thermodynamic non-idealities in mixture separations using zeolites and metal-organic frameworks

Rajamani Krishna[a,*], Jasper M. van Baten[b], Richard Baur[a,1]

[a] Van 't Hoff Institute for Molecular Sciences, University of Amsterdam, Science Park 904, 1098 XH Amsterdam, The Netherlands
[b] AmsterCHEM, Almería, Spain

ARTICLE INFO

Keywords:
Molecular clustering
Hydrogen bonding
Segregation
Transient membrane permeation
Fixed bed adsorbers
Maxwell-Stefan diffusion

ABSTRACT

The Ideal Adsorbed Solution Theory (IAST) is widely used for the estimation of the mixture adsorption equilibrium, and for quantitative modeling of separations using microporous adsorbents and membranes. With the aid of Configurational-Bias Monte Carlo (CBMC) simulations, the accuracy of the IAST estimations of the component loadings for mixture adsorption equilibrium is investigated for a wide variety of mixtures in zeolites, and metal-organic frameworks (MOFs). The IAST estimations are found to be of inadequate accuracy under two different scenarios: (1) when there is molecular clustering, caused by strong hydrogen bonding between the adsorbates, as is the case for water/alcohol, alcohol/alcohol, and alcohol/aromatic mixtures, and (2) there is inhomogeneous, segregated, distribution of adsorbates within the pore network, caused by preferential siting and locations of guest molecules. For both these scenarios, quantitative agreement with CBMC simulations of mixture adsorption is realized by application of the Real Adsorbed Solution Theory (RAST) by incorporation of activity coefficients, suitably parameterized by the Wilson model for the excess Gibbs free energy of adsorption.

The important consequences of thermodynamic non-idealities are underscored for transient operations of fixed bed adsorbers for which the IAST and RAST may anticipate opposite sequences of component breakthroughs. For water/alcohol separations in membrane pervaporation processes, the permeation selectivities predicted by the IAST and RAST may differ by an order of magnitude.

1. Introduction

Microporous adsorbents such as zeolites, and metal-organic frameworks (MOFs) offer energy-efficient alternatives to conventional separation technologies such as distillation, absorption, extraction and fractional crystallization. Though research on the development of novel adsorbents have been largely triggered by CO_2 capture, alkene/alkane, and alkyne/alkene separations, more recent researches have unveiled the vast potential of microporous adsorbents and membranes for water/alcohol, alcohol/alcohol, alcohol/aromatics, aliphatic/aromatic, and hydrocarbon isomers separations [1–18]. The successful design and development of fixed bed adsorbers, and membrane devices utilizing such microporous materials is crucially dependent on robust and accurate procedures for estimation of mixture adsorption equilibria.

Within microporous crystalline materials, the guest molecules exist in the adsorbed phase. The Gibbs adsorption equation [19], written in differential form as $Ad\pi = \sum_{i=1}^{n} q_i d\mu_i$, is the appropriate starting point to describe adsorption equilibrium. The quantity A is the surface area per kg of framework, with units of m^2 per kg of the framework of the crystalline material; q_i is the molar loading of component i in the adsorbed phase usually expressed in the units of moles per kg of framework; μ_i is the molar chemical potential of component i. The spreading pressure π has the same units as surface tension, i.e. N m^{-1}. The chemical potential of component i in the adsorbed phase, μ_i, equals that in the bulk fluid phase. If the partial fugacities in the bulk fluid phase are f_i, we have $d\mu_i = RTd\ln f_i$. In the Ideal Adsorbed Solution Theory (IAST) of Myers and Prausnitz [20], the partial fugacities in the bulk fluid mixture are related to the mole fraction in the adsorbed phase $x_i = \frac{q_i}{q_1 + q_2 + \ldots q_n}$ by the analogue of Raoult's law for vapor-liquid equilibrium, i.e. $f_i = P_i^0 x_i; \quad i = 1,2, \ldots n$ where P_i^0 is the pressure for sorption of every component i, which yields the same spreading pressure, π for each of the pure components, as that for the mixture:

$$\frac{\pi A}{RT} = \int_0^{P_1^0} \frac{q_1^0(f)}{f} df = \int_0^{P_2^0} \frac{q_2^0(f)}{f} df = \int_0^{P_3^0} \frac{q_3^0(f)}{f} df = \ldots \quad (1)$$

The units of $\frac{\pi A}{RT}$, also called the adsorption potential [21], are mol kg^{-1}. If the *pure* component adsorption $q_i^0(f)$ isotherm are described

* Corresponding author.
E-mail addresses: jasper@amsterchem.com (J.M. van Baten), richard.baur@shell.com (R. Baur).
[1] Current affiliation: Shell Global Solutions International BV, Amsterdam, The Netherlands.

https://doi.org/10.1016/j.micromeso.2018.03.013
Received 12 October 2017; Accepted 12 March 2018
Available online 16 March 2018
1387-1811/

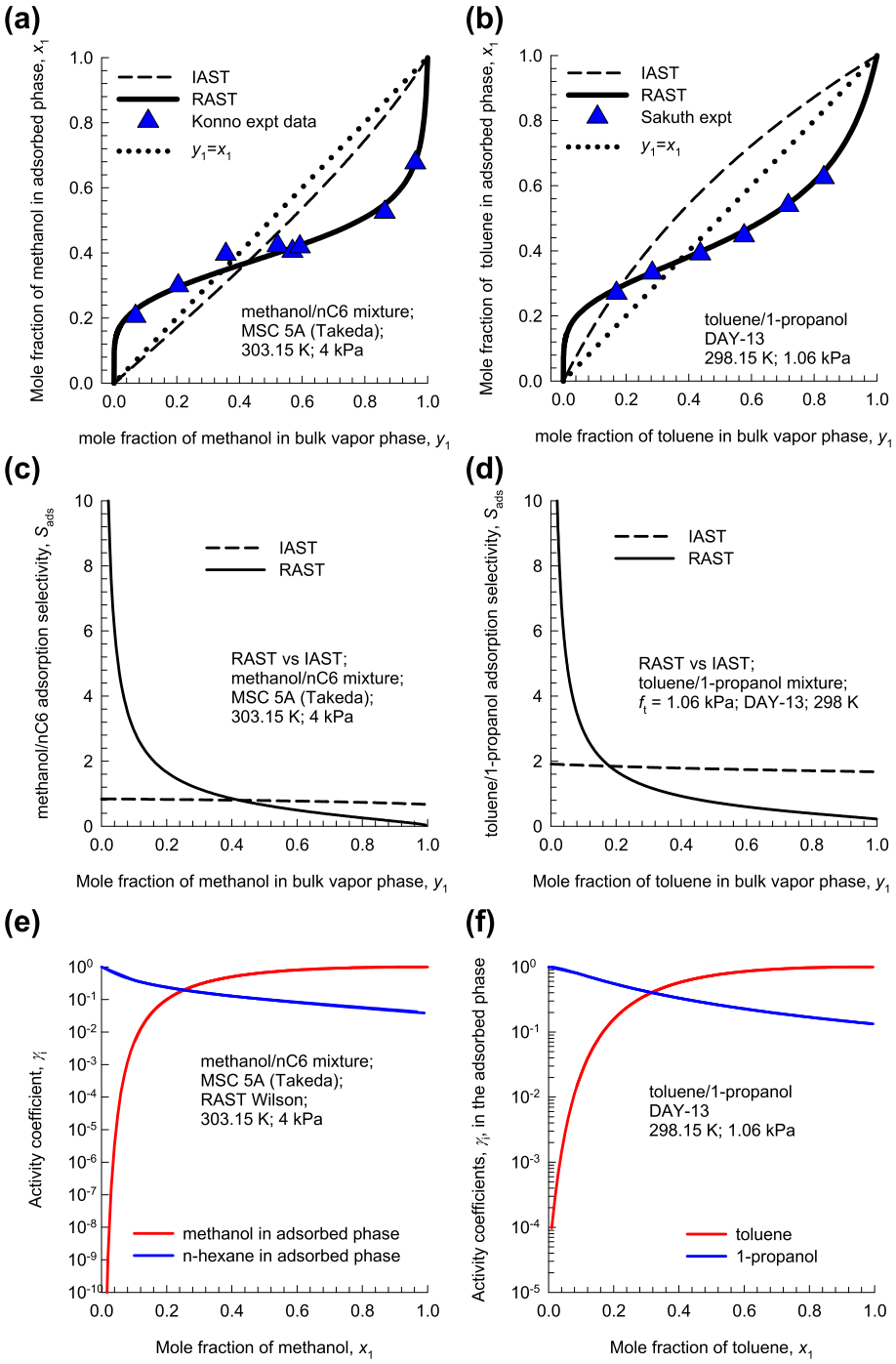

Fig. 1. (a) Experimental data of Konno et al. [23] for adsorption of methanol/n-hexane (nC6) mixtures in MSC-5A (Takeda) at 4 kPa and 303.15 K. (b) Experimental data of Sakuth et al. [24] of toluene/1-propanol mixtures in DAY-13 (dealuminated Y zeolite) at T = 298 K and total pressure p_t = 1.06 kPa (c, d) Comparison of the IAST and RAST calculations of the adsorption selectivity, S_{ads}. (e, f) RAST calculations of the activity coefficients in the adsorbed phase as a function of the mole fraction of component 1 in the bulk vapor phase, y_1. All computational details are provided in the Supplementary Material.

by, say, the dual-site Langmuir-Freundlich isotherm, each of the integrals in Equation (1) can be evaluated analytically. For specified partial fugacities in the bulk fluid phase, f_i, these constraints may be solved simultaneously, to yield the set of values of the adsorbed phase mole fractions, x_i, and P_i^0, all of which must satisfy Equation (1). The corresponding values of the integrals using these as upper limits of integration must yield the same value of $\frac{\pi A}{RT}$ for each component.

A key assumption of the IAST is that the enthalpies and surface areas of the adsorbed molecules do not change upon mixing. If the total mixture loading is q_t, the area covered by the adsorbed mixture is $\frac{A}{q_t}$ with units of m^2 (mol mixture)$^{-1}$. Therefore, the assumption of no surface area change due to mixture adsorption translates as follows

$$\frac{A}{q_t} = \frac{Ax_1}{q_1^0(P_1^0)} + \frac{Ax_2}{q_2^0(P_2^0)} + \cdots \frac{Ax_n}{q_n^0(P_n^0)} \tag{2}$$

The total mixture loading is q_t is then calculated from

$$q_t \equiv q_1 + q_2 \ldots + q_n = \frac{1}{\frac{x_1}{q_1^0(P_1^0)} + \frac{x_2}{q_2^0(P_2^0)} + \ldots + \frac{x_n}{q_n^0(P_n^0)}} \tag{3}$$

The IAST is widely used in practice for the calculation of the mixture

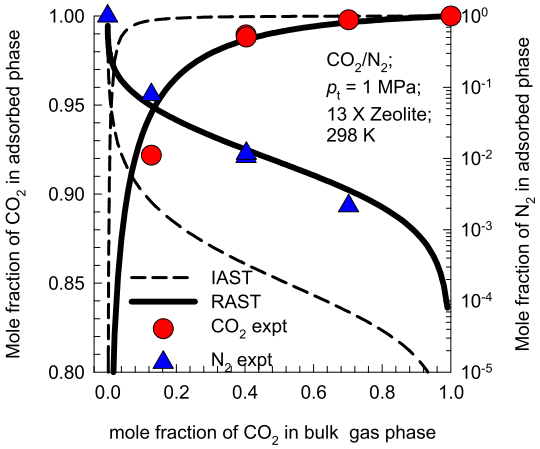

Fig. 2. Experimental data of Hefti et al. [25] for adsorbed phase mole fractions, x_i, for CO_2/N_2 mixture adsorption in 13X zeolite at 298 K and total pressure p_t = 1 MPa, as function of the mole fraction of CO_2 in the bulk gas phase. The continuous solid lines are the estimations using RAST. All computational details are provided in the Supplementary Material.

adsorption equilibrium in microporous adsorbents [4,22]. To set the scene for this article and define its objectives, let us consider a number of published sets of experimental data on binary mixture adsorption.

Fig. 1a presents data of Konno et al. [23] for adsorption of methanol/n-hexane (nC6) mixtures in Takeda Molecular Sieve Carbon MSC-5A at a total vapor pressure of 4 kPa and T = 303.15 K; the adsorbed phase mole fraction of methanol is plotted as a function the mole fraction of methanol in the bulk vapor phase. It is noteworthy that mixture adsorption exhibits azeotropic behavior. The phenomenon of azeotropic mixture adsorption is characterized by the equality of mole fractions in the bulk vapor phase and in the adsorbed phase, $y_1 = x_1$. For bulk vapor phase methanol fractions lower than 0.5, the adsorbed phase is richer in methanol, the adsorbate with the smaller molecular size. However, for bulk vapor phase richer in methanol, the adsorbed phase is richer in n-hexane, the adsorbate with the larger molecular size and stronger binding strength.

Fig. 1b presents experimental data of Sakuth et al. [24] for toluene/1-propanol mixture adsorption in DAY-13 (dealuminated Y zeolite, with Faujasite topology) at T = 298 K and total pressure p_t = 1.06 kPa. For bulk vapor phase toluene fractions lower than 0.2, the adsorbed phase is richer in toluene, the component with the stronger binding strength but lower saturation capacity. However, for bulk vapor phase richer in

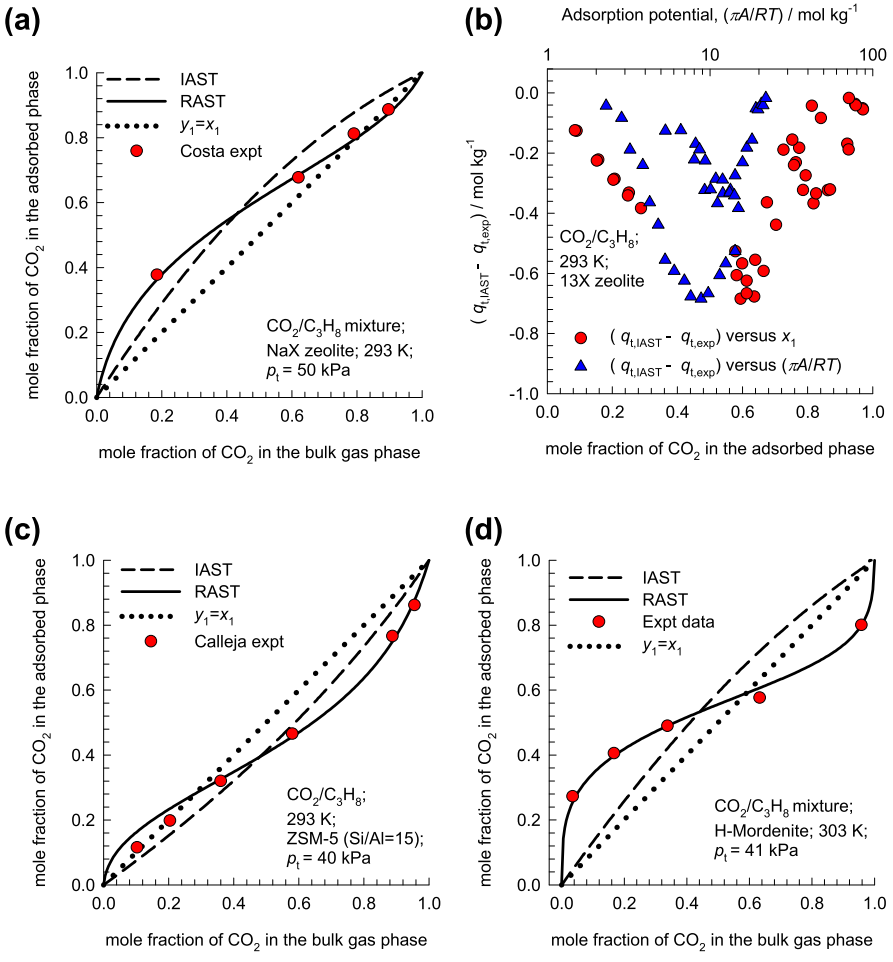

Fig. 3. Analysis of experimental data for adsorption of binary CO_2/C_3H_8 mixtures in cation exchanged zeolites. (a) Experimental data of Costa et al. [28] for adsorption of CO_2/C_3H_8 mixtures at 293 K and a total pressure of 50 kPa in NaX (= 13 X) zeolite at. (b) Analysis of experimental data of Siperstein and Myers [21] for adsorption of CO_2/C_3H_8 mixtures in NaX zeolite and 293 K of their paper. The differences in the estimation of the total mixture loading, $q_{t,IAST}$ from the experimental data, $q_{t,exp}$ is plotted as function of the adsorbed phase mole fraction of CO_2, determined experimentally, in the bottom axis, and the adsorption potential, $\frac{\pi A}{RT}$, in the top axis. (c) Experimental data of Calleja et al. [36] for adsorption of CO_2/C_3H_8 mixtures at 293 K and 40 kPa in ZSM-5 (with MFI topology) zeolite with Si/Al ratio = 15. (d) Experimental data of Talu and Zwiebel [33] for adsorption of CO_2/C_3H_8 mixtures at 303 K and total gas phase pressure p_t = 41 kPa in H-MOR (= H-Mordenite). The IAST estimates are indicated as dashed lines and the continuous solid lines are the RAST model calculations; all input data and computational details are provided in the Supplementary Material.

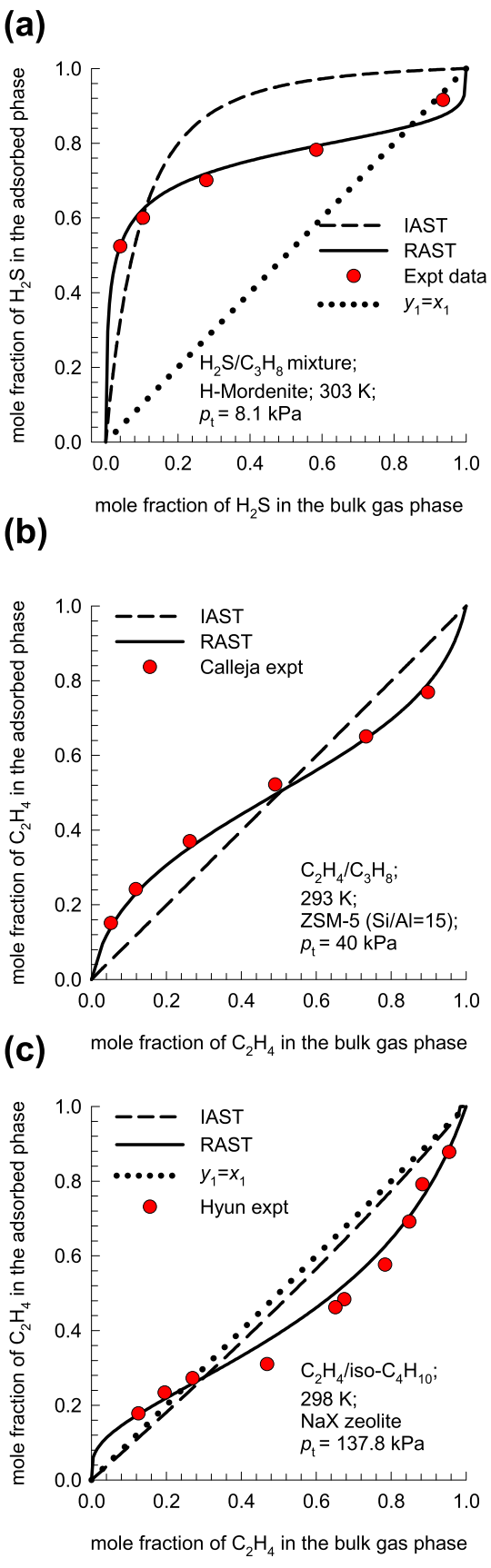

Fig. 4. (a) Experimental data of Talu and Zwiebel [33] for adsorption H_2S/C_3H_8 mixtures at 303 K and p_t = 8.1 kPa in H-MOR. (b) Experimental data of Calleja et al. [36] for adsorption of C_2H_4/C_3H_8 mixtures at 293 K and p_t = 40 kPa in ZSM-5 (with MFI topology) zeolite with Si/Al ratio = 15. (c) Experimental data of Hyun and Danner [35] for adsorption of C_2H_4/iso-C_4H_{10} mixtures at 298 K and p_t = 137.8 kPa in 13X zeolite. The IAST estimates are indicated as dashed lines and the continuous solid lines are the RAST model calculations; all input data and computational details are provided in the Supplementary Material.

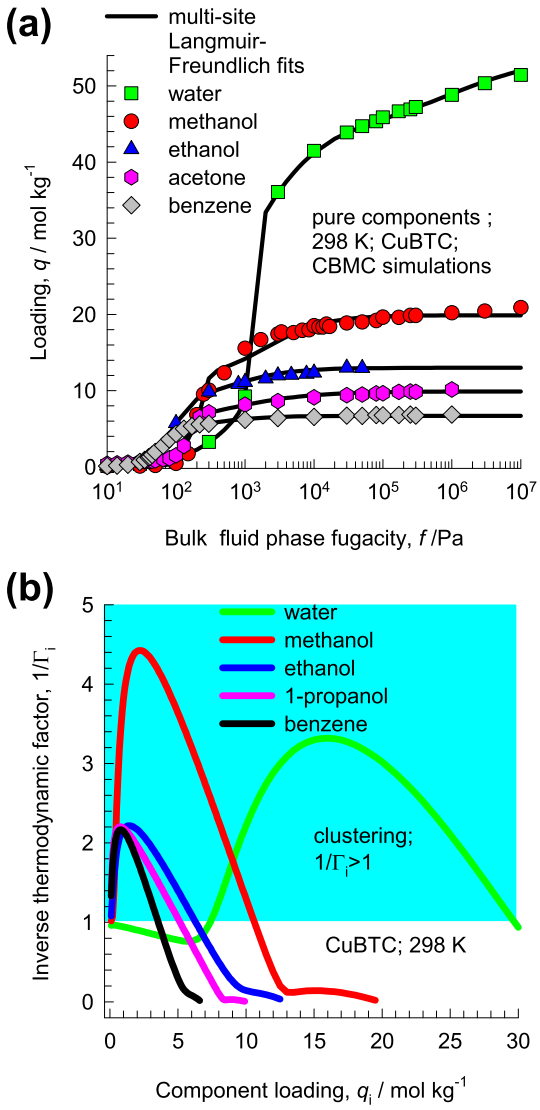

Fig. 5. (a) CBMC simulation data [2,3] for unary isotherms of water, methanol, ethanol, acetone, and benzene in CuBTC at 298 K. The continuous solid lines are 3-site (for water) or 2-site Langmuir-Freundlich model fits. (b) The inverse thermodynamic factor, $1/\Gamma_i$, plotted as a function of the molar loadings. The isotherm fit parameters, and all other computational details are provided in the Supplementary Material.

toluene, the adsorbed phase is richer in 1-propanol that has the lower binding strength but higher saturation capacity.

The IAST estimations of the adsorbate composition, x_1, and the adsorption selectivity, S_{ads}, defined by

$$S_{ads} = \frac{q_1/q_2}{y_1/y_2} = \frac{x_1/x_2}{y_1/y_2} \tag{4}$$

are shown by the dashed lines in Fig. 1c and d. For both systems, the IAST anticipates that the adsorption selectivities are practically independent of composition; no selectivity reversals observed in the

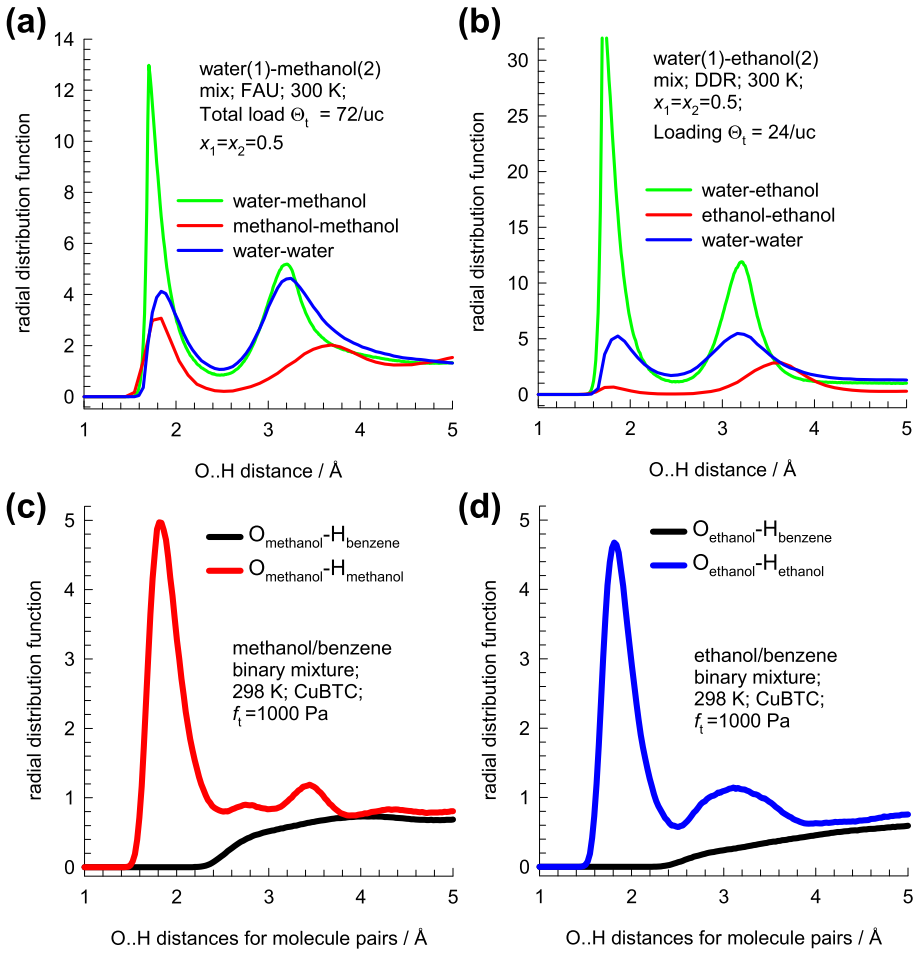

Fig. 6. CBMC simulation data [2,3,46] for RDFs for (a) water/methanol in FAU (b) water/ethanol mixtures in DDR, (c) methanol/benzene mixtures in CuBTC and (d) ethanol/benzene mixtures in CuBTC.

experiments are anticipated. Clearly, one or more of the key assumptions underlying the IAST are not fulfilled in the two experimental data sets in Fig. 1.

Cation-exchanged zeolites such as NaY, NaX, ZSM-5, LTA-4A, LTA-5A, SAPO-34, and H-MOR are commonly employed for separation of CO_2/alkane, CO_2/H_2, and CO_2/N_2 mixtures [17,18,21,25–31], The selective adsorption of CO_2 is ascribable to strong Coulombic interactions with the extra-framework cations; this principle also applies to selective adsorption of H_2S-bearing mixtures [32]. Fig. 2 presents experimental data of Hefti et al. [25] for CO_2/N_2 mixture adsorption in 13X zeolite at a total pressure p_t = 1 MPa, and T = 298 K; the adsorbed phase mole fractions, x_i, are plotted as function of the mole fraction of CO_2 in the bulk gas phase. The IAST (shown by the dashed lines) overestimates the adsorbed phase mole fraction of CO_2 loading, and severely underestimates the mole fraction of N_2; consequently, the adsorption selectivities calculated using the IAST are overly optimistic.

The experimental data of Costa et al. [28] for adsorption of CO_2/C_3H_8 mixtures in NaX (= 13X) zeolite at 293 K clearly demonstrates the occurrence of the phenomenon of azeotropic adsorption, i.e. $y_1 = x_1$, that is not anticipated by IAST estimates; see Fig. 3a. For CO_2/C_3H_8/NaX adsorption, the differences in the total mixture loadings, $q_t = q_1 + q_2$, between IAST estimations and experimental data of Siperstein and Myers [21] are plotted in Fig. 3b, as function of the adsorbed phase mole fraction of CO_2, x_1, as the bottom x-axis. The plot shows that the deviation of IAST estimations from experimental data is not uniquely determined by x_1. From Fig. 3b it appears that $q_{t,IAST} - q_{t,\exp}$ is also dependent on the adsorption potential, $\frac{\pi A}{RT}$, that is plotted as the top x-axis. It is particularly noteworthy that the deviations tend to zero as $\frac{\pi A}{RT} \to 0$. The adsorption of CO_2/C_3H_8 mixtures in other cation exchanged zeolites such as ZSM-5 (Si/Al = 15) and H-Mordenite also exhibit the phenomena of azeotropic adsorption; see Fig. 3c and d.

The experimental data of Talu and Zwiebel [33] for adsorption H_2S/C_3H_8 mixtures in H-Mordenite exhibit both azeotropic adsorption and exceedingly large deviations from IAST estimates for H_2S-rich gas mixtures; see Fig. 4a.

Cation-exchanged zeolites are also effective for separation of alkene/alkane mixtures [17,21,28,33–37]; the adsorption selectivity in favor of the unsaturated alkene is due to stronger binding and π-electron exchanges with the extra-framework cations. The experiments of Calleja et al. [36] for C_2H_4/C_3H_8/ZSM-5, and of Hyun and Danner [35] for C_2H_4/iso-C_4H_{10}/NaX show the occurrence of azeotropic adsorption and concomitant failure of the IAST for quantitative predictions; see Fig. 4b and c.

The primary objective of this article is to highlight the shortcomings of the IAST, such as that witnessed in Figs. 1–4 for a wide variety of guest/host combinations; Wu and Sircar [38] provide further literature references on failures of the IAST estimations. The origins of failure of the IAST estimations are explored, and elucidated. We aim to demonstrate that the failures of IAST have fundamentally different origins, depending on the guest/host combinations. In view of the paucity of experimental data sets on mixture adsorption, we utilize data based on Configurational-Bias Monte Carlo (CBMC) simulations on unary isotherms and mixture adsorption equilibrium. The CBMC simulation techniques are well established, and have been applied extensively for adsorption in zeolites and MOFs [39–41]. The secondary objective is to

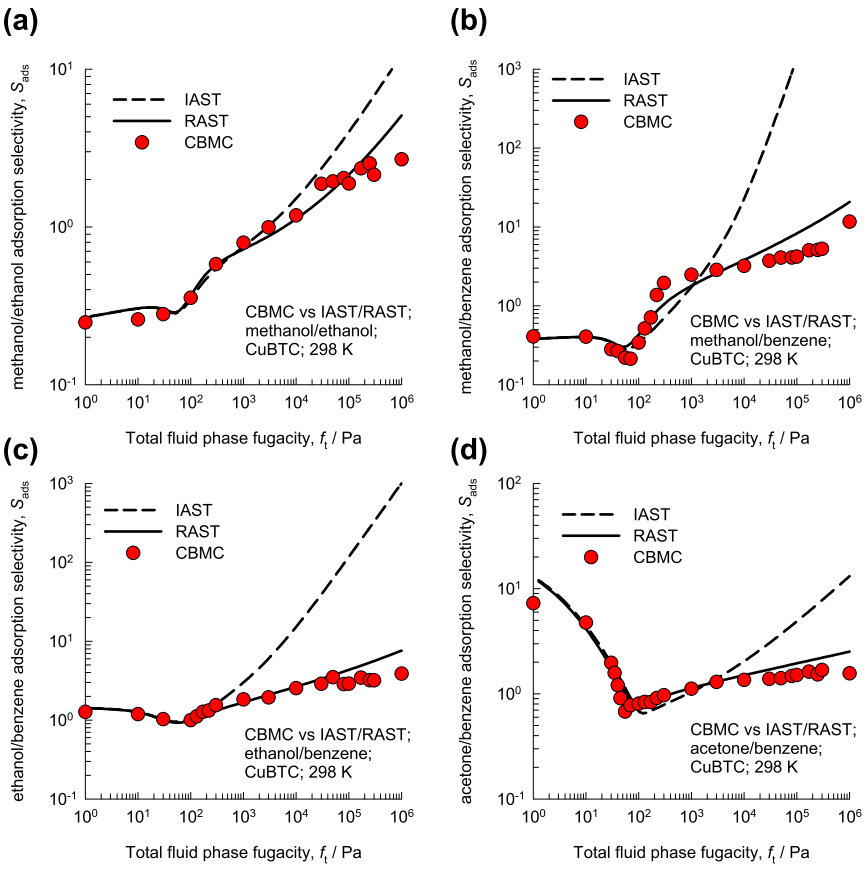

Fig. 7. Comparison of CBMC simulation data on the adsorption selectivities [2,3] (indicated by symbols) for (a) methanol/ethanol, (b) methanol/benzene, (c) ethanol/benzene, and (d) acetone/benzene mixtures in CuBTC at 298 K with IAST (dashed lines), and RAST (continuous solid lines) calculations. The partial fugacities in the bulk fluid phase are taken to be equal, i.e. $f_1 = f_2$. The Wilson parameters, and all other computational details are provided in the Supplementary Material.

investigate the magnitude of departures from IAST by calculations of the activity coefficients in the adsorbed phase, and use of the Real Adsorbed Solution Theory (RAST) [3,21,33,42,43]. We aim to show that the modeling of activity coefficients must take due account of the dependence on the adsorption potential, $\frac{\pi A}{RT}$, as witnessed in Fig. 3b. The tertiary objective is to underscore, with the aid of a number of illustrative examples, the severe consequences of thermodynamic non-idealities for mixture separations in fixed bed adsorbers and membrane devices.

The Supplementary Material accompanying this publication provides (a) detailed structural information on all of the zeolites, and MOFs analyzed and discussed in the article, (b) details of the IAST, and RAST methodologies and calculations for mixture adsorption equilibria, (c) input data on unary isotherm fits for the wide variety of guest/host combinations examined in this article, (d) detailed comparisons of CBMC simulations of mixture adsorption equilibrium, with IAST and RAST calculations, (e) details of Maxwell-Stefan modeling of mixture permeation across microporous membranes, and (f) simulation methodology for transient breakthroughs in fixed bed adsorbers. Also uploaded are video animations demonstrating the phenomena of molecular clustering, and preferential location of guest molecules in different host materials.

We start with a brief summary of the model used to describe thermodynamic non-idealities.

2. Modeling activity coefficients for mixture adsorption

In the RAST, the partial fugacity of any component in the bulk fluid phase is related to the mole fraction x_i in the adsorbed phase by introduction of activity coefficients describing non-idealities in the adsorbed phase

$$f_i = P_i^0 x_i \gamma_i \tag{5}$$

The determination of the adsorbed phase mole fractions x_i using equation (5) requires an appropriate model for the activity coefficients defined by the excess Gibbs free energy for binary mixture adsorption

$$\frac{G^{excess}}{RT} = x_1 \ln(\gamma_1) + x_2 \ln(\gamma_2) \tag{6}$$

In view of the data presented in Fig. 3b, the Wilson model for activity coefficients, for example, must include the influence of the adsorption potential [3,20,21,33,42,43].

$$\ln(\gamma_1) = \left(1 - \ln(x_1 + x_2\Lambda_{12}) - \frac{x_1}{x_1 + x_2\Lambda_{12}} - \frac{x_2\Lambda_{21}}{x_2 + x_1\Lambda_{21}}\right)\left(1 - \exp\left(-C\frac{\pi A}{RT}\right)\right)$$
$$\ln(\gamma_2) = \left(1 - \ln(x_2 + x_1\Lambda_{21}) - \frac{x_2}{x_2 + x_1\Lambda_{21}} - \frac{x_1\Lambda_{12}}{x_1 + x_2\Lambda_{12}}\right)\left(1 - \exp\left(-C\frac{\pi A}{RT}\right)\right) \tag{7}$$

In equation (7), C is a constant with the units kg mol^{-1}. The introduction of $\left(1 - \exp\left(-C\frac{\pi A}{RT}\right)\right)$ imparts the correct limiting behaviors $\gamma_i \to 1; \quad f_t \to 0$ for the activity coefficients in the Henry regime. As pore saturation conditions are approached, this correction factor tends to unity, $\left(1 - \exp\left(-C\frac{\pi A}{RT}\right)\right) \to 1$. We note, in passing, that this correction factor is often ignored in the RAST implementations in some published works [34,44,45]. The choice of $\Lambda_{12} = \Lambda_{21} = 1$ in Equation (7) yields unity values for the activity coefficients.

The excess reciprocal loading for the mixture can be defined as

$$\left(\frac{1}{q_t}\right)^{excess} = \frac{1}{q_t} - \left(\frac{x_1}{q_1^0} + \frac{x_2}{q_2^0(P_2^0)}\right) \tag{8}$$

The excess reciprocal loading for the mixture can be related to the partial derivative of the Gibbs free energy with respect to the adsorption potential at constant composition

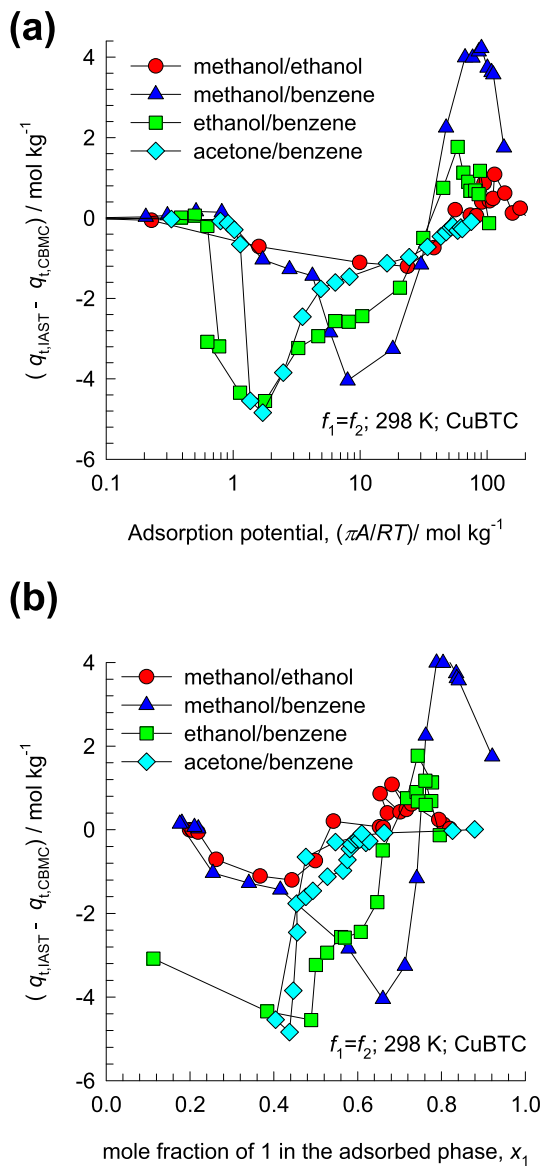

Fig. 8. (a, b) Dependence of $q_{t,IAST} - q_{t,CBMC}$ on (a) adsorption potential, $\frac{\pi A}{RT}$, and (b) adsorbed phase mole function of component 1 determined from CBMC simulation, for methanol/ethanol, methanol/benzene, ethanol/benzene, and acetone/benzene mixtures in CuBTC at 298 K. The input data and all other computational details are provided in the Supplementary Material.

$$\left(\frac{1}{q_t}\right)^{excess} = \left.\frac{\partial\left(\frac{G^{excess}}{RT}\right)}{\partial\left(\frac{\pi A}{RT}\right)}\right|_{T,x} = [-x_1 \ln(x_1 + x_2\Lambda_{12}) - x_2 \ln(x_2 + x_1\Lambda_{21})]C \exp\left(-C\frac{\pi A}{RT}\right) \tag{9}$$

For calculation of the total mixture loading we need to replace Equation (3) by

$$q_t \equiv q_1 + q_2 = \frac{1}{\frac{x_1}{q_1^0(P_1^0)} + \frac{x_2}{q_2^0(P_2^0)} + [-x_1 \ln(x_1 + x_2\Lambda_{12}) - x_2 \ln(x_2 + x_1\Lambda_{21})]C \exp\left(-C\frac{\pi A}{RT}\right)} \tag{10}$$

The continuous solid lines in Fig. 1a and b represent RAST calculations for methanol/nC6/MSC-5A, and toluene/1-propanol/DAY-13 systems with fitted Wilson parameters: (a) $\Lambda_{12} = 1.2$; $\Lambda_{21} = 68$; $C = 0.15\,\text{kg mol}^{-1}$, and (b) $\Lambda_{12} = 0.52$; $\Lambda_{21} = 12.2$; $C = 1.1\,\text{kg mol}^{-1}$. The corresponding values of the activity coefficients, calculated using the fitted parameters, are shown in Fig. 1e and f. For both systems, for bulk vapor phase mole fractions, $y_1 < 0.2$, the activity of component 1, methanol or toluene, is reduced by several orders of magnitude below unity.

A different approach to introduce the correction factor $\left(1 - \exp\left(-C\frac{\pi A}{RT}\right)\right)$ into the Wilson equations has been adopted by Hefti et al. [25] for developing a RAST description of adsorption equilibrium for CO_2/N_2 mixtures in ZSM-5 and 13X zeolites for a variety of pressures ranging to 1 MPa. In their approach the Wilson coefficients are corrected as follows

$$\Lambda_{ij} = (\Lambda_{ij}^0 - 1)\left(1 - \exp\left(-C\frac{\pi A}{RT}\right)\right) + 1 \tag{11}$$

Use of the modified Wilson parameters as defined in equation (11) ensures the correct limiting behaviors $\gamma_i \to 1$; $\frac{\pi A}{RT} \to 0$ for the activity coefficients.

The extension of the foregoing analysis to *n*-component mixtures is straightforward; see Supplementary Material for details.

3. Manifestation of molecular clustering induced by hydrogen bonding

In recent years there have been several molecular simulation and experimental studies on unary and mixture adsorption characteristics of polar compounds such as water, methanol, and ethanol in a variety of microporous materials; on the basis of these studies there is clear evidence of clustering of the guest molecules caused due to hydrogen bonding [2,3,46–53]. An important signature of the occurrence of molecular clustering is that the unary isotherms do not follow simple Langmuirian behavior; rather, the isotherms exhibit step-like characteristics, as illustrated in Fig. 5a by CBMC simulations [2,3] for unary isotherms of water, methanol, ethanol, acetone, and benzene in CuBTC (= $Cu_3(BTC)_2$ with BTC = 1,3,5-benzenetricarboxylate, also known as HKUST-1). The isotherm characteristics can only be adequately modelled using multi-site Langmuir-Freundlich model fits, shown by the continuous solid lines. The manifestation of molecular clustering is revealed by calculations of the inverse thermodynamic factor, $1/\Gamma_i$, defined by

$$\frac{1}{\Gamma_i} \equiv \frac{\partial \ln q_i}{\partial \ln f_i} = \frac{f_i}{q_i}\frac{\partial q_i}{\partial f_i} \tag{12}$$

Fig. 5b show that the values of $1/\Gamma_i$ exceeds unity for a range of molar loadings, q_i; this is indicated by the shaded region. In order to fully appreciate the importance of $1/\Gamma_i > 1$, we consider the simple case for which the adsorbed phase loading follows a single-site Langmuir isotherm $q_i = q_{i,sat}\frac{b_i f_i}{1 + b_i f_i}$, that yields $\frac{1}{\Gamma_i} = 1 - \theta_i = \theta_V$, the fractional vacancy that is always lower than unity, $1/\Gamma_i \leq 1$. When there is no molecular clustering, increasing the loading, q_i, by increasing the bulk fluid phase fugacity, leads to *linear decrease* in the number of vacant sites. For the data presented in Fig. 5b, it appears that for a range of loadings, there is an *increase* in the number of vacant sites for a range of component loadings, q_i. This is the direct consequence of the fact that a molecular cluster, say a dimer, occupies less surface area that two unclustered molecules [51], consequently, the key assumption made in the derivation of the IAST, *viz.* Equation (2), is invalidated.

To demonstrate that molecular clustering may be induced by hydrogen bonding between molecular pairs, we examine the radial distribution functions (RDFs) for distances between all combinations of O···H ("hydrogen bonds") pairs. For adsorption of water/methanol, and water/ethanol mixtures, Fig. 6a and b presents the RDFs for O-H bonding of water-water, alcohol-alcohol, and water-alcohol pairs in FAU and DDR zeolites. The first peak of the RDF manifests at distances smaller than 2 Å for all three molecular pairs, that is characteristic of

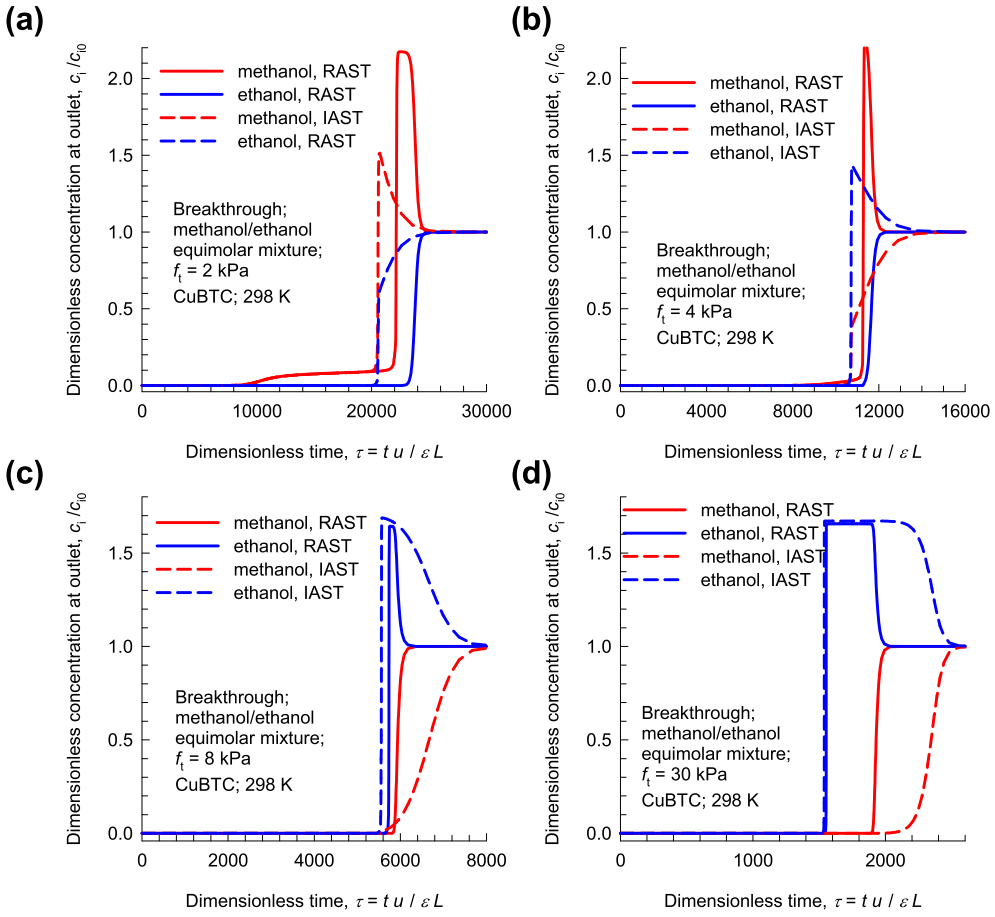

Fig. 9. Transient breakthrough simulations of 50/50 methanol/ethanol feed mixtures in fixed bed adsorbed packed with CuBTC at 298 K, operating at total fluid mixture fugacities: (a) f_t = 2 kPa, (b) f_t = 4 kPa, (c) f_t = 8 kPa, and (d) f_t = 30 kPa. The *x*-axes represent the dimensionless time, $\tau = \frac{tu}{L\varepsilon}$, obtained by dividing the actual time, *t*, by the characteristic time, $\frac{L\varepsilon}{u}$, where *L* is the length of adsorber, *u* is the superficial fluid velocity, ε is the bed voidage [14,15,65,67]. The *y*-axes are the molar concentrations at the exit of the fixed bed, normalized with respect to the concentrations in the feed mixture at the inlet, $\frac{c_i}{c_{i0}}$. The Wilson parameters, and all other computational details are provided in the Supplementary Material.

hydrogen bonding [54]. Furthermore, we note that the first peak value is significantly higher for the water-alcohol pair, indicating that clustering between water-alcohol pairs is the strongest. Fig. 6c and d presents the RDFs for methanol/benzene, and ethanol/benzene mixtures in CuBTC [2,3]. These data show that the H-bonding is exclusively between alcohol/alcohol pairs.

A visual appreciation of molecular clustering phenomena can be gained from video animations created from Molecular Dynamics (MD) simulations of water in DDR (Video 1), methanol in DDR (Video 2), ethanol in DDR (Video 3), methanol in FER (Video 4), methanol/ethanol in FER (Video 5), and methanol/ethanol in CHA (Video 6).

Supplementary video related to this article can be found at http://dx.doi.org/10.1016/j.micromeso.2018.03.013.

4. Consequence of hydrogen bonding on selectivity reversals in fixed bed adsorbers

CBMC simulations for adsorption of binary methanol(1)/ethanol(2), methanol(1)/benzene(2), ethanol(1)/benzene(2), and acetone(1)/benzene(2) mixtures in CuBTC at 298 K were carried out with equal partial fugacities of components 1 and 2 in the bulk fluid phase, i.e. $f_1 = f_2$ [2,3]. The adsorption selectivity of component 1 with respect to component 2 are plotted in Fig. 7a,b,c, d as function of the total fluid mixture fugacity, $f_t = f_1 + f_2$. For all four binary mixtures, the CBMC mixture simulations show that selectivity reversals occur. With increasing f_t, the selectivity is in favor of the component with the higher saturation capacity; from unary isotherm data in Fig. 5a, the saturation loadings for methanol, ethanol, acetone and benzene are, respectively, 19.9, 13, 9.9, and 6.7 mol kg^{-1}. The selectivity reversal is ascribable to entropy effects favoring the smaller molecule that packs more efficiently within the pores and have a higher saturation capacity [2–4,16]. Though the IAST correctly anticipates the entropy effects and selectivity reversals for all four mixtures, the agreement with CBMC mixture data becomes progressively inaccurate with increased values of bulk fluid fugacity, f_t. The failure of the IAST to accurately match CBMC mixture simulations, as presented in Fig. 7, is most likely due to the phenomenon of molecular clustering, induced by hydrogen bonding [2,3]. Due to cluster formation one of the key assumptions, *viz.* Equation (2), is violated; this reasoning also provides the theoretical foundation for the large deviations of IAST estimates of the adsorption selectivities for methanol/n-hexane in CuBTC observed in the experiments of van Assche et al. [55]; see analysis in Fig. S55.

The departures of IAST estimates of the total mixture loadings from CBMC mixture simulation data, $q_{t,IAST} - q_{t,CBMC}$, depend both on the

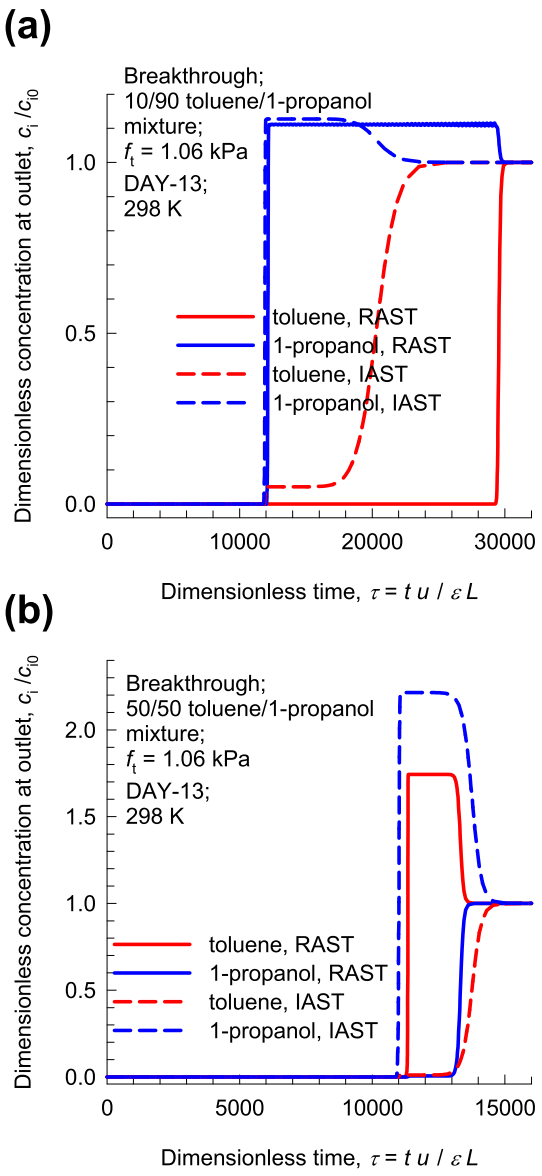

Fig. 10. (a, b) Transient breakthrough simulations of toluene(1)/1-propanol(2) feed mixtures in fixed bed adsorbed packed with DAY-13, operating at 298 K and p_t = 1.06 kPa. The feed mixture compositions are: (c) y_1 = 0.1, and (d) y_1 = 0.5. All computational details are provided in the Supplementary Material.

composition of the adsorbed phase and the adsorption potential, $\frac{\pi A}{RT}$. This is verified by the plots in Fig. 8a and b; these plots underscore the importance of introducing the $\left(1-\exp\left(-C\frac{\pi A}{RT}\right)\right)$ into the Wilson equations for activity coefficients, and are in line with the experimental data of Siperstein and Myers [21] plotted in Fig. 3b. For all four mixtures, the departures of IAST from CBMC simulations tend to vanish as $\frac{\pi A}{RT} \to 0$.

Quantifying the adsorbed phase non-idealities with fitted Wilson parameters Λ_{12}, Λ_{21}, and C, the RAST calculations offer significant quantitative improvements over the corresponding IAST calculations; see the continuous solid lines in Fig. 7a,b,c,d.

In order to underscore the significance of departures of activity coefficients from unity on mixture separations, Fig. 9 presents transient breakthrough simulations of 50/50 methanol/ethanol feed mixtures in fixed bed adsorbed packed with CuBTC, operating at 298 K and total fluid mixture fugacities: (a) f_t = 2 kPa, (b) f_t = 4 kPa, (c) f_t = 8 kPa, and (d) f_t = 30 kPa (see Supplementary Material for modeling details).

For operation at f_t = 2 kPa, both IAST and RAST anticipate that the

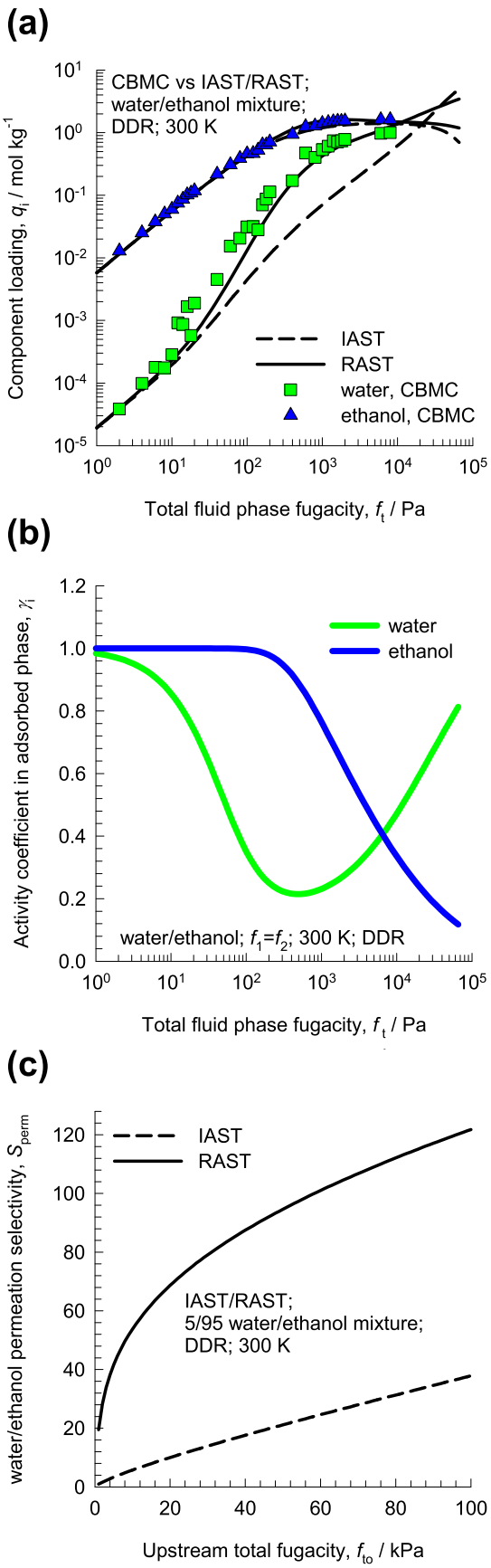

(caption on next page)

Fig. 11. (a) CBMC simulation data [46,62] for adsorption of water/ethanol mixture in DDR zeolite at 300 K. Also shown are the IAST (dashed lines), and RAST (continuous solid lines) estimations of component loadings. (b) RAST calculations of the activity coefficients for water and ethanol. (c) Comparison of the IAST and RAST calculations of the permeation selectivity, $S_{perm} = \frac{N_1/N_2}{f_{10}/f_{20}}$. The isotherm fits, and Wilson parameters are provided in the Supplementary Material.

more strongly adsorbed component is the longer chain alcohol, and the shorter chain alcohol is rejected. This separation is "normal", and dictated by the stronger binding of the longer chain alcohol. For operations at $f_t = 8$ kPa, and $f_t = 30$ kPa, entropy effects cause the shorter chain alcohol to be preferentially adsorbed and the longer chain ethanol is "rejected" [4,16]. In view of the larger differences in the breakthrough times of ethanol and methanol, the IAST predicts that the production of pure ethanol is larger than those estimated by use of the RAST. For operations at $f_t = 4$ kPa, the differences in the breakthrough characteristics determined with IAST and RAST implementations are particularly striking. The IAST anticipates that methanol is the component that is preferentially adsorbed, but the RAST predicts the selective adsorption of ethanol.

Experimental confirmation of the selectivity reversals, such as that witnessed in Fig. 9c and d, are provided in the experiments reported by van Assche et al. [55] for transient breakthroughs of methanol/n-hexane mixtures in fixed beds packed with CuBTC. Remy et al. [56] report transient breakthroughs experiments of for ethanol/1-propanol, and ethanol/1-hexanol mixtures in a fixed bed adsorber packed with SAPO-34 (that has the same structural topology as CHA zeolite); the component that is eluted first from the adsorber bed is the component with the lower saturation capacity [55,56]. The rationalization of these experimental data can be traced to the entropy effects that favor the component that packs more efficiently under pore saturation conditions [4,16].

Fig. 10a and b presents transient breakthrough simulations of toluene(1)/1-propanol(2) feed mixtures in fixed bed adsorbed packed with DAY-13, operating at 298 K and $p_t = 1.06$ kPa with two different feed mixture compositions: (a) $y_1 = 0.1$, and (b) $y_1 = 0.5$. For operation with feed mixture composition $y_1 = 0.1$, both IAST and RAST anticipate that the more strongly adsorbed component is toluene that has the stronger binding with the framework; during the time interval between breakthroughs of 1-propanol and toluene, nearly pure 1-propanol can be collected. We also note that the IAST implementation produces distended breakthroughs. The IAST calculations result in a shorter time interval between breakthroughs and, consequently, the productivity of pure 1-propanol is significantly lower than that calculated using the RAST. Due to higher adsorption selectivity anticipated by RAST (cf. Fig. 1d), the transient breakthroughs are sharper using the RAST and

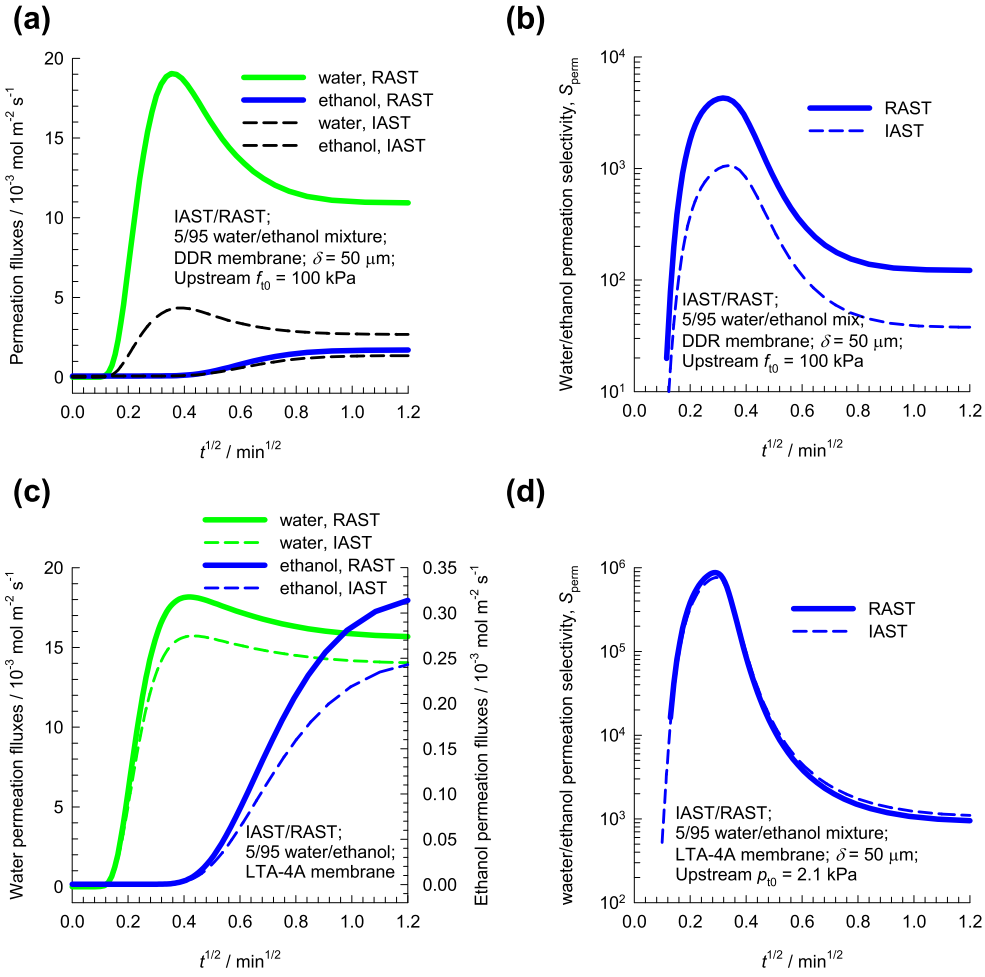

Fig. 12. (a, c) Permeation fluxes, and (b, d) watter/ethanol permeation selectivities for transient permeation of 5/95 water(1)/ethanol(2) mixtures across (a, b) DDR membrane at 300 K, and (b) LTA-4A membrane at 333 K. The dashed lines represent calculations based on IAST estimations of phase equilibrium at the upstream and downstream faces; the continuous solid lines are the corresponding estimations using RAST. The isotherm fits, and Wilson parameters are provided in the Supplementary Material.

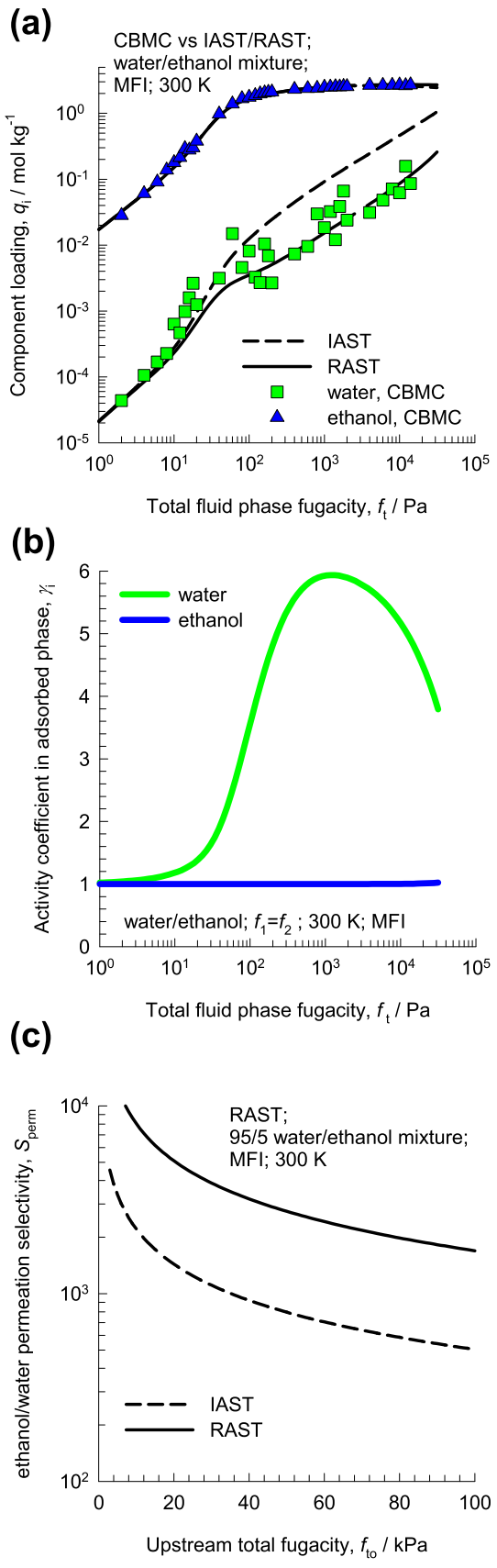

Fig. 13. (a) CBMC simulation data [46,62] for adsorption of water(1)/ethanol (2) mixture in MFI zeolite at 300 K. Also shown are the IAST (dashed lines), and RAST (continuous solid lines) estimations of component loadings. (b) RAST calculations of the activity coefficients for water and ethanol. (c) Comparison of the IAST and RAST calculations of the permeation selectivity, $S_{perm} = \frac{N_2/N_1}{f_{20}/f_{10}}$. The isotherm fits, and Wilson parameters are provided in the Supplementary Material.

the productivity of 1-propanol is significantly higher.

The situation is completely different for transient breakthroughs with an equimolar feed mixture, $y_1 = 0.5$. In this case, the RAST anticipates that 1-propanol is selectively adsorbed and toluene is rejected. The IAST, on the other hand, anticipates that toluene is selectively adsorbed and pure 1-propanol can be produced in the adsorption cycle. Inclusion of thermodynamic non-idealities reverses the separation capability in this case.

5. Consequences of hydrogen bonding for water/alcohol separations with zeolite membranes

For water/alcohol separations, CHA [57,58], DDR [59], LTA-4A [60], and MFI zeolites [45,61] are promising materials for use in membrane separation devices. We now demonstrate the strong influence of hydrogen bonding effects on water/ethanol separations with zeolite membranes [3,4,46–48,54,62–64].

Fig. 11a presents CBMC simulations for adsorption of equimolar (partial fugacities $f_1 = f_2$) water/ethanol mixture in DDR zeolite at 300 K. In the Henry regime of adsorption, the water loading is significantly below that of ethanol. However, we note that at total fugacities, $f_t = f_1 + f_2 = 1 \times 10^4$ Pa, the loading of water equals that of ethanol; this trend is a consequence of entropy effects that favor water with the higher saturation capacity [4]. The dashed solid lines are the IAST calculations using pure component isotherm fits. The IAST calculations are able to provide a reasonably good description of mixture adsorption equilibrium for $f_t < 10$ Pa. For $f_t > 10$ Pa, there are significant quantitative deviations between IAST calculations and CBMC simulations of water loadings in the mixture. With fitted Wilson parameters, the RAST calculations (shown by the continuous solid lines) provide good match with the CBMC simulated loadings (cf. Fig. 11a); the corresponding calculations of the activity coefficients are shown in Fig. 11b. Both activity coefficients are reduced below unity; this reduction is significantly stronger for water.

Using the Maxwell-Stefan model for membrane permeation [65,66] (see Supplementary Material for the modeling details), Fig. 11c presents calculations of the permeation selectivity for 5/95 water/ethanol mixtures with varying total fugacity, $f_{t0} = f_{10} + f_{20}$, in the upstream compartment:

$$S_{perm} = \frac{N_1/N_2}{f_{10}/f_{20}} \tag{13}$$

In equation (13), the N_i are the trans-membrane molar fluxes and f_{i0} are the partial fugacities in the upstream compartment. Taking due account of the non-idealities in mixture adsorption equilibrium at the fluid/membrane interfaces, the RAST estimates of S_{perm} are about three times higher than those predicted by the IAST.

During transient approach to steady-state, the water flux displays overshoots and the permeation selectivities reach values about 10–100 times the steady-state value; see Fig. 12a and b. The origin of the water flux overshoot can be traced to thermodynamic coupling in the permeation fluxes [67], induced the thermodynamic correction factors Γ_{ij}:

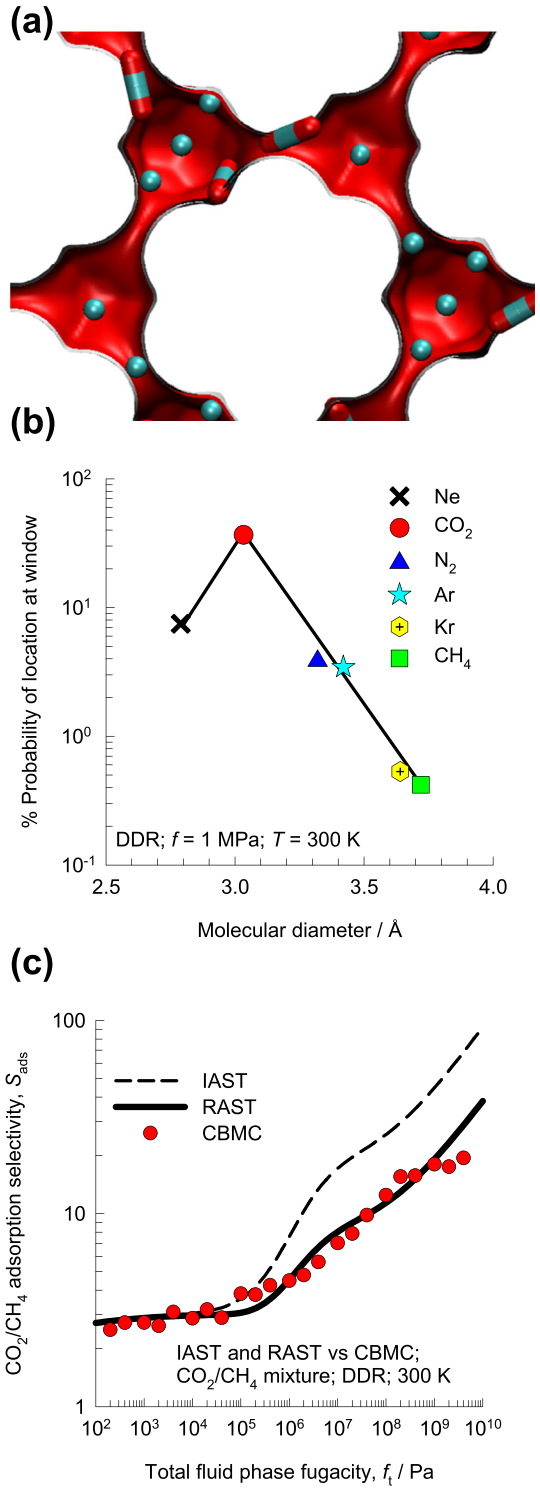

Fig. 14. (a) Computational snapshot showing the location of CO_2 and CH_4 within the cage/window structure of DDR zeolite [71]. (b) % probability for adsorption of component in the window region of DDR. (c) CBMC simulations for the CO_2/CH_4 adsorption selectivities for equimolar CO_2/CH_4 mixtures in DDR compared with IAST and RAST calculations. The isotherm fits, and Wilson parameters are provided in the Supplementary Material.

$$\frac{q_i}{RT}\frac{d\mu_i}{dz} = \sum_{j=1}^{n} \Gamma_{ij}\frac{dq_j}{dz}; \qquad \Gamma_{ij} = \frac{q_i}{f_i}\frac{\partial f_i}{\partial q_j}; \qquad i, j = 1, \ldots n \tag{14}$$

The thermodynamic correction factors Γ_{ij} can be determined from the mixture adsorption equilibrium model description. If the thermodynamic coupling effects are ignored, and the matrix $[\Gamma]$ is assumed to equal the identity matrix $[I]$, the overshoot disappears [67].

For transient permeation of 5/95 water/ethanol mixtures across LTA-4A membranes, the S_{perm} values are about three orders of magnitude higher than those at steady-state; see Fig. 12c and d. The deliberate exploitation of high water/ethanol permeation selectivities during the initial stages of transience remains a practical challenge.

Hydrophobic MFI zeolite membranes have potential use in the recovery of ethanol from dilute aqueous solutions [45,61]. In order to demonstrate the significance of thermodynamic non-idealities on the MFI membrane permeation characteristics, we analyze water(1)/ethanol(2) mixture permeation across all-silica MFI zeolite membrane at 300 K. Fig. 13a presents CBMC simulations for adsorption of equimolar (partial fugacities $f_1 = f_2$) water/ethanol mixture in MFI zeolite at 300 K. In the Henry regime of adsorption, the water loading is significantly below that of ethanol. The estimations of the IAST are particularly unsatisfactory for water at total fugacities $f_t = f_1 + f_2$ in excess of 100 Pa. Introduction of activity coefficients, and use of the RAST provides a good match with the CBMC simulated loading; see Fig. 13a and b. It is noteworthy that the activity coefficient of water is significantly higher than unity for a range of bulk fluid phase fugacities. The ethanol/water membrane permeation selectivities, estimated using the RAST are about an order of magnitude higher than those estimated using the IAST; see Fig. 13c.

6. Preferential perching of CO_2 at window regions and within pockets

For separation of CO_2 from gaseous mixtures containing CH_4, cage-type zeolites such as DDR (see pore landscape in Fig. 14a), CHA, LTA, and ERI are of practical interest [17,26,68–70]. These materials consist of cages separated by narrow windows, in the 3.3–4.5 Å range. The selectivity of separation of CO_2 is dictated by both adsorption and diffusion characteristics. For adsorption of CO_2/CH_4 mixtures, CBMC simulations [71] show that the window regions of cage-type zeolites has a significantly higher proportion of CO_2 than within the cages. For all four zeolites, CO_2 has the highest probability, about 30%–40%, of locating at the window regions; the data for DDR presented in Fig. 14b. Video animations demonstrating the perching of CO_2 in the window regions are demonstrated for CO_2/CH_4 in LTA (Video 7), and CO_2/CH_4 in ERI (Video 8).

Supplementary video related to this article can be found at http://dx.doi.org/10.1016/j.micromeso.2018.03.013.

A key assumption of the IAST is that the components in the adsorbed phase are homogeneously and uniformly distributed within the zeolite or MOF. Due to the segregated nature of mixture adsorption and preferential perching of CO_2 at the window regions, the IAST is unable to predict the mixture loadings accurately. This is evidenced by comparisons of the CO_2/CH_4 adsorption selectivities for equimolar CO_2/CH_4 mixtures in DDR compared with IAST calculations; see Fig. 14c. The IAST calculation assumes that CH_4 molecules compete with *all* of the CO_2, making no allowance for segregation. Due to segregation effects, the competition faced by CH_4 molecules within the cages, where they almost exclusively reside, is *smaller* than that in the entire pore space. The IAST anticipates a stiffer competition between CO_2 and CH_4 as it assumes a uniform distribution of composition; consequently, the

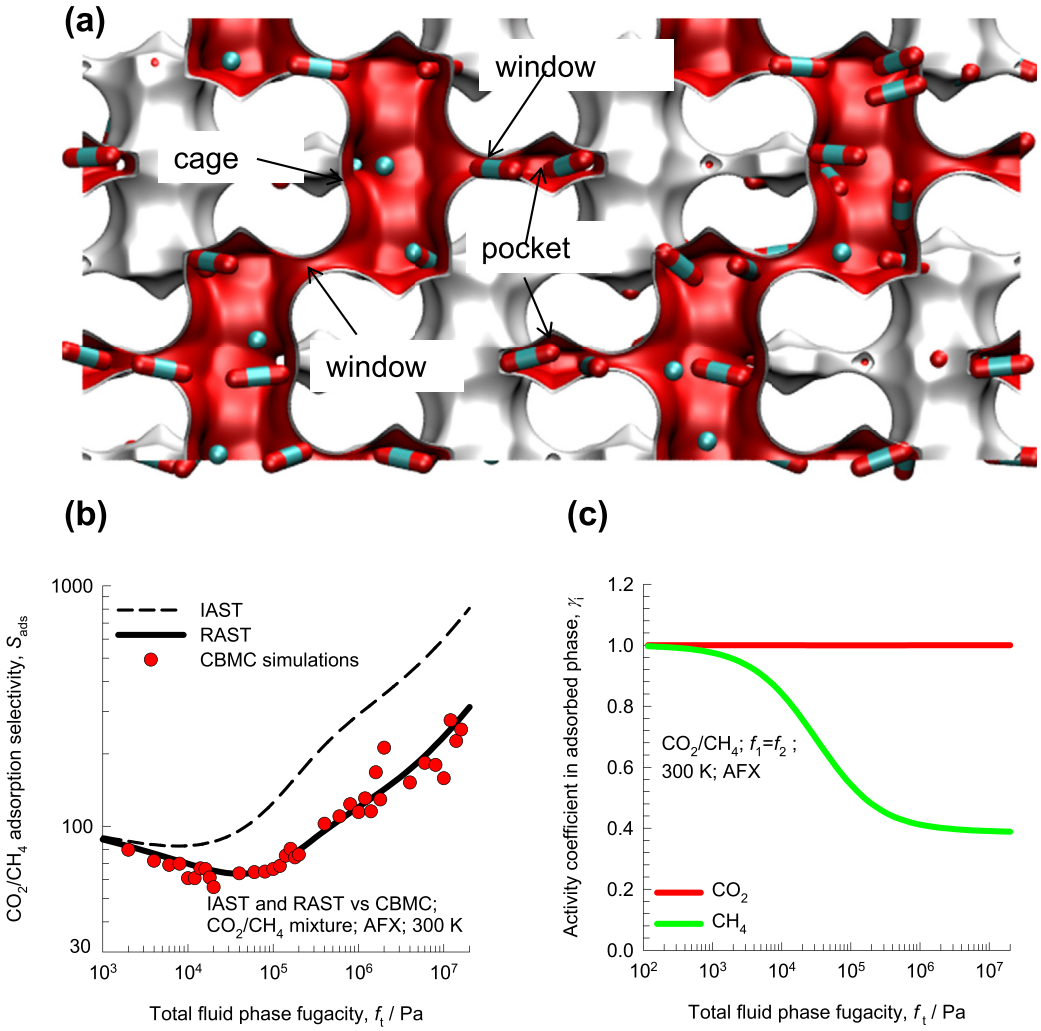

Fig. 15. (a) Computational snapshot showing the location of CO_2 and CH_4 within the cage/window structure of AFX zeolite [18,68]. (b) Comparison CO_2/CH_4 adsorption selectivities obtained from CBMC with IAST and RAST estimations. (c) RAST calculations of the activity coefficients γ_i for CO_2 and CH_4. All computational details are provided in the Supplementary Material. The isotherm fits, and Wilson parameters are provided in the Supplementary Material.

separation selectivity is *over*estimated. Use of the RAST, with fitted Wilson parameters is able to capture the non-ideality effects due to mixture adsorption.

For CO_2/CH_4, and CO_2/N_2 mixture separations using AFX zeolite, two different types of segregation effects are distinguishable [18]. CO_2 molecules preferentially locate at the window regions and also in small pockets that are connected to the cages; see computational snapshot in Fig. 15a, along with the animations in Video 9 (CO_2/CH_4 in AFX), and Video 10 (CO_2/N_2 in AFX). The CO_2/CH_4 adsorption selectivities determined from CBMC simulations range from 70 to 500. As evidenced in Fig. 15b, the selectivities are significantly overestimated by the IAST for the same reasons as elucidated above for DDR zeolite. Due to the much stronger adsorption of CO_2 the component loadings in the mixture are hardly influenced by the presence of the more weakly adsorbed CH_4; the activity coefficient of CO_2 is unity over the entire range of fugacities. On the other hand, the activity coefficient of CH_4 fall significantly below unity with increasing bulk fluid fugacities; see Fig. 15c.

Supplementary video related to this article can be found at http://dx.doi.org/10.1016/j.micromeso.2018.03.013.

MOR zeolite (Mordenite) consists of 12-ring (7.0 Å × 6.5 Å) 1D channels, connected to 8-ring (5.7 Å × 2.6 Å) pockets. Computational snapshot (cf. Fig. 16a) of the location of molecules for CO_2/CH_4 mixture adsorption show that CO_2 gets preferentially ensconced in the side-pockets. Fig. 16b presents a comparison of the estimations using the IAST and RAST with CBMC simulations of component loadings of equimolar (partial fugacities $f_1 = f_2$) CO_2/CH_4 mixtures in MOR zeolite at 300 K. We note that the IAST under-predicts the loading of the more weakly adsorbed CH_4 in the CO_2/CH_4 mixture. The conventional IAST calculation assumes that CH_4 molecules compete with *all* of the CO_2, making no allowance for segregation. Due to segregation effects the competition faced by CH_4 molecules within the 12-ring channels, where they almost exclusively reside, is *smaller* than that in the entire pore space. The IAST anticipates a stiffer competition between CO_2 and CH_4 as it assumes a uniform distribution of composition; consequently the separation selectivity is *over*estimated; see Fig. 16c.

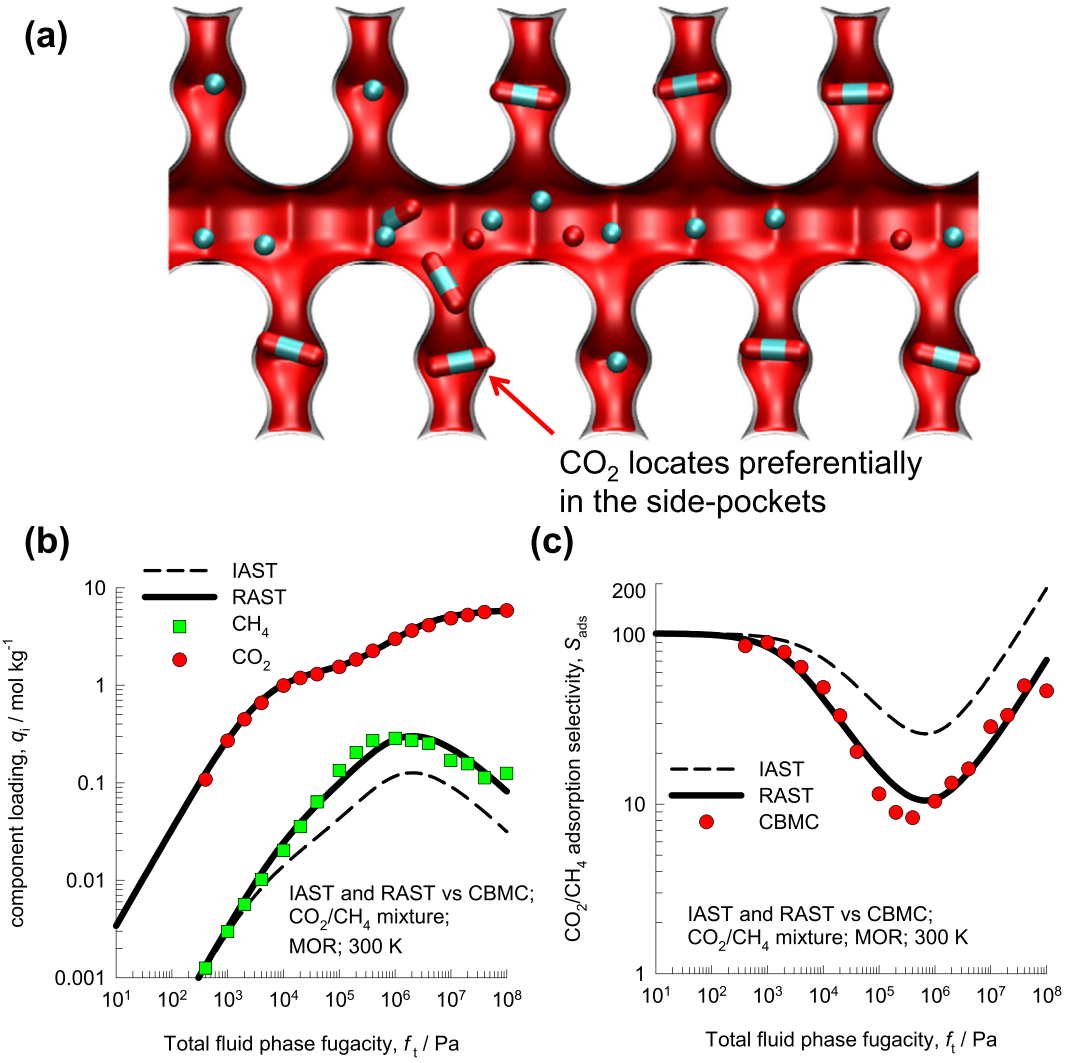

Fig. 16. (a) Comparison of the estimations using the IAST and RAST with CBMC simulations [79,80] of component loadings of equimolar (partial fugacities $f_1 = f_2$) CO_2/CH_4 mixtures in MOR zeolite at 300 K. (b) RAST calculations of the component activity coefficients γ_i, for CO_2 and CH_4. (c) Comparison CO_2/CH_4 adsorption selectivities obtained from CBMC with IAST and RAST estimations. The isotherm fits, and Wilson parameters are provided in the Supplementary Material.

7. Congregation around extra-framework cations

For CO_2 capture from natural gas at high pressures, predominantly containing CH_4, NaX zeolite is a potential adsorbent. NaX zeolite, commonly called 13X zeolite, has 106 Si, 86 Al, and 86 Na^+ per unit cell with Si/Al = 1.23. Due to strong coulombic interactions of CO_2 with the extra-framework Na^+ ions, the selectivity is strongly in favor of CO_2. There is a tendency of CO_2 molecules to congregate around the cations; as evidenced by the snapshot in Fig. 17a; this results in an inhomogeneous distribution of adsorbates CO_2 and CH_4 within the cages of NaX zeolite. Neutron diffraction data [72] establish that CO_2 molecules attach strongly via O atoms to the unsaturated Mg^{2+} atoms of MgMOF-74, causing an inhomogeneous distribution of adsorbates within the hexagonal channels.

The IAST calculation assumes that CH_4 molecules compete with *all* of the CO_2, making no allowance for congregation. Due to congregation effects the competition faced by CH_4 molecules within the cages is *smaller* than that in the entire pore space. The IAST anticipates a stiffer competition between CO_2 and CH_4 as it assumes a uniform distribution of composition; consequently the CO_2/CH_4 selectivity is *over*estimated. This is confirmed by comparisons of the IAST estimations of CO_2/CH_4 adsorption selectivities with CBMC simulation data [68]; see Fig. 17b. CO_2 congregation effects cause the activity coefficient of CH_4 to fall significantly below unity with increase fluid phase fugacity, f_t; see Fig. 17c.

Congregation effects may be expected to become decreasingly significant as the number of extra-framework cations is reduced. To demonstrate this, Fig. 17d presents a comparison CBMC CO_2/CH_4 adsorption selectivities determined from CBMC simulations at 300 K for all-silica FAU (192 Si, 0 Al, 0 Na^+, Si/Al = ∞), NaY (138 Si, 54 Al, 54 Na^+, Si/Al = 2.56), and NaX (106 Si, 86 Al, 86 Na^+, Si/Al = 1.23) zeolites with IAST estimations. For all-silica FAU, the IAST estimates are in perfect agreement with CBMC simulations. The agreement of IAST estimates with CBMC simulated data becomes progressively worse with decreasing Si/Al ratios.

The propensity of CO_2 molecules to congregate around the Na^+

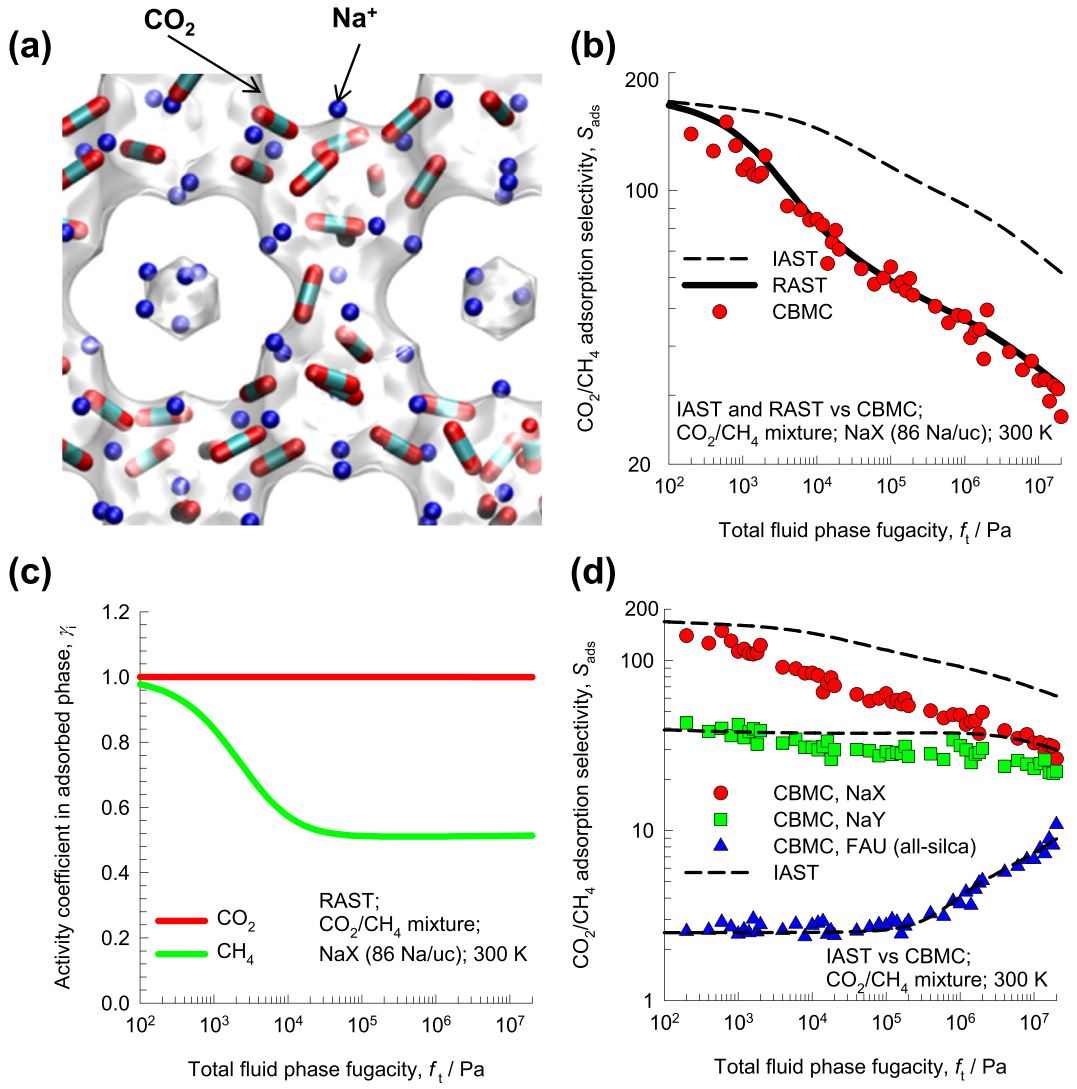

Fig. 17. (a) Computational snapshot illustrating congregation of CO_2 molecules around the Na^+ cations [68]. (b) Comparison CO_2/CH_4 adsorption selectivities for CO_2/CH_4 mixtures in NaX zeolite at 300 K, obtained from CBMC simulations [68] with IAST and RAST estimations. (c) RAST calculations of the component activity coefficients γ_i, for CO_2 and CH_4. (d) Comparison CBMC CO_2/CH_4 adsorption selectivities determined from CBMC simulations 300 K for all-silica FAU (192 Si, 0 Al, 0 Na^+, Si/Al = ∞), NaY (138 Si, 54 Al, 54 Na^+, Si/Al = 2.56), and NaX (106 Si, 86 Al, 86 Na^+, Si/Al = 1.23) zeolites with IAST estimations. The isotherm fits, and Wilson parameters are provided in the Supplementary Material.

cations also explains the failure of IAST as evidenced for CO_2/N_2/NaX (cf. Fig. 2), CO_2/C_3H_8/NaX (cf. Fig. 3a and b), CO_2/C_3H_8/ZSM-5 (cf. Fig. 3c), and CO_2/C_3H_8/H-MOR (cf. Fig. 3d).

Hydrogen sulfide (H_2S) and unsaturated alkenes also congregate around extra-framework cations, and unsaturated metal sites of MOFs undergoing π-coordination [73,74]; this rationalizes the failure of the IAST as evidenced for H_2S/C_3H_8/H-MOR (cf. Fig. 4a), C_2H_4/C_3H_8/ZSM-5 (cf. Fig. 4b), and C_2H_4/iso-C_4H_{10}/NaX (cf. Fig. 4c).

In order to demonstrate the consequences of non-idealities induced by congregation of CO_2 around the extra-framework Na^+ ions, we analyze the separation of 85/15 $CO_2(1)/C_3H_8(2)$ feed mixtures in fixed bed packed with NaX zeolite operating at 293 K, at a total pressure, p_t = 50 kPa for which the y_1-x_1 experimental data exhibit selectivity reversal (cf. Fig. 3a). The transient breakthroughs with IAST and RAST implementations are compared in Fig. 18a. Use of the RAST for mixture adsorption anticipates that C_3H_8 is preferentially adsorbed, and purified CO_2 can be recovered during the early transience. On the other hand, using the IAST estimates of mixture adsorption equilibrium, we note that CO_2 is preferentially adsorbed, and C_3H_8 is rejected during initial transience.

Fig. 18b compares transient breakthrough simulations of 17/83 CO_2/C_3H_8 feed mixtures in fixed bed packed with H-MOR, using the IAST and RAST estimates for mixture adsorption equilibrium. In this case, the RAST implementation anticipates CO_2-selective adsorption, and rejection of C_3H_8. Use of the IAST severely underestimates the productivity of pure C_3H_8.

Fig. 18c presents transient breakthrough simulations of 10/20 C_2H_4/C_3H_8 feed mixtures in fixed bed packed adsorber ZSM-5 (Si/Al ratio = 15) zeolite, operating at total pressure, p_t = 30 kPa and 293 K. The transient breakthroughs using the RAST estimation of mixture

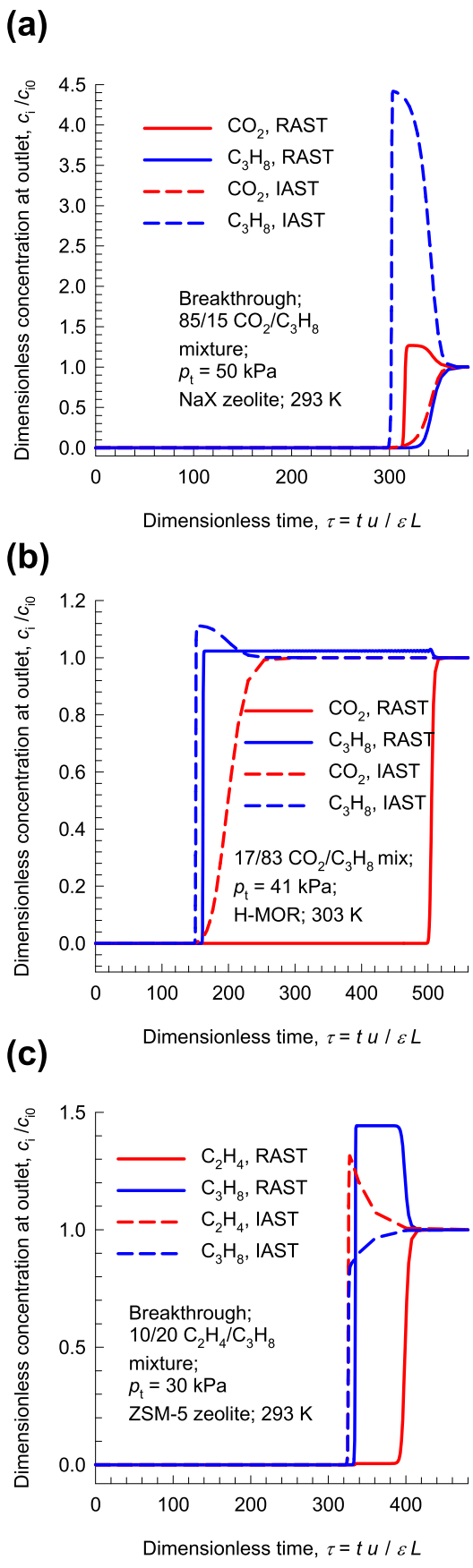

Fig. 18. Transient breakthrough simulations of (a) 85/15 CO_2/C_3H_8 feed mixtures in fixed bed adsorber packed with NaX zeolite, operating at 293 K and p_t = 50 kPa, (b) 17/83 CO_2/C_3H_8 feed mixtures in fixed bed packed with H-MOR, operating at 303 K and p_t = 41 kPa, and (c) 10/20 C_2H_4/C_3H_8 feed mixtures in fixed bed packed adsorber ZSM-5 (Si/Al ratio = 15) zeolite, operating at 293 K and p_t = 30 kPa. All data inputs computational details are provided in the Supplementary Material.

adsorption equilibrium shows a clear separation, with preferential adsorption of C_3H_8. In sharp contrast, use of the IAST model shows that both guest molecules breakthrough at the same time, and no separation is achievable.

8. Preferential location of branched alkanes at channel intersections of MFI zeolite

A different type of segregated adsorption manifests for adsorption of mixtures of linear and branched alkanes within the intersecting channels of MFI zeolite. The linear alkanes can locate anywhere within the channel network, but due to configurational considerations, the branched alkanes prefer to locate at the channel intersections that offer more "leg room" [41,65,75–77]. This is illustrated by the computational snapshots in Fig. 19a,b for adsorption of n-butane(nC4)/iso-butane(iC4), and n-hexane(nC6)/2-methylpentane(2 MP) mixtures.

Due to the inhomogeneity in the distribution of linear and branched alkanes, the IAST estimations are not in perfect agreement with CBMC simulations of mixture adsorption equilibrium; see Fig. 19c,d. The experimental data of Titze et al. [76] for nC4/iC4, and nC6/2 MP mixture adsorption confirm that entropy effects result in exclusion of branched alkanes at high loadings. For quantitative modeling, the mixture adsorption equilibrium, the use of the RAST, shown by the continuous solid lines in Fig. 19c,d, is essential.

Fig. 20a presents simulations of the transient uptake of nC4/iC4 mixtures in MFI crystals. The linear *n*-butane has a mobility that is about 1–2 orders of magnitude higher than that of the branched isomer because of subtle configurational differences; this has been established PFG NMR experiments of Fernandez et al. [78]. Configurational-entropy effects also serve to prefer the adsorption of the linear isomer [76]. The continuous solid lines in Fig. 20a are simulation results using the RAST, that include the influence of thermodynamic coupling. The nC4 loading overshoot is analogous to the water flux overshoots witnessed in Fig. 12 for water/ethanol permeation across DDR and LTA-4A membranes. In order to demonstrate that the nC4 overshoots are due to thermodynamic coupling effects, the dotted lines in Fig. 20a are simulations in which the matrix of thermodynamic correction factors is taken to be the identity matrix $\begin{bmatrix} \Gamma_{11} & \Gamma_{12} \\ \Gamma_{21} & \Gamma_{22} \end{bmatrix} \rightarrow \begin{bmatrix} 1 & 0 \\ 0 & 1 \end{bmatrix}$; no nC4 overshoots are detected in this scenario, as explained in earlier work [67].

The synergy between diffusion and adsorption also manifests for nC6/2 MP mixture separations in MFI zeolite; transient uptake of nC6/2 MP mixtures in MFI crystals displays an overshoot in the nC6 loading; see Fig. 20b. The nC6 overshoot is confirmed in the experimental data reported by Titze et al. [76].

Analogous segregation effects also manifest for adsorption of CH_4/iC4, C_2H_6/iC4, C_3H_8/iC4, CH_4/Benzene, C_2H_4/Benzene, and C_3H_6/Benzene mixtures in MFI zeolite; see the analysis of non-ideality effects in Figs. S131–S140.

9. Conclusions

The following major conclusions emerge from the discussions and analysis of adsorption of a variety of mixtures in zeolites and MOFs

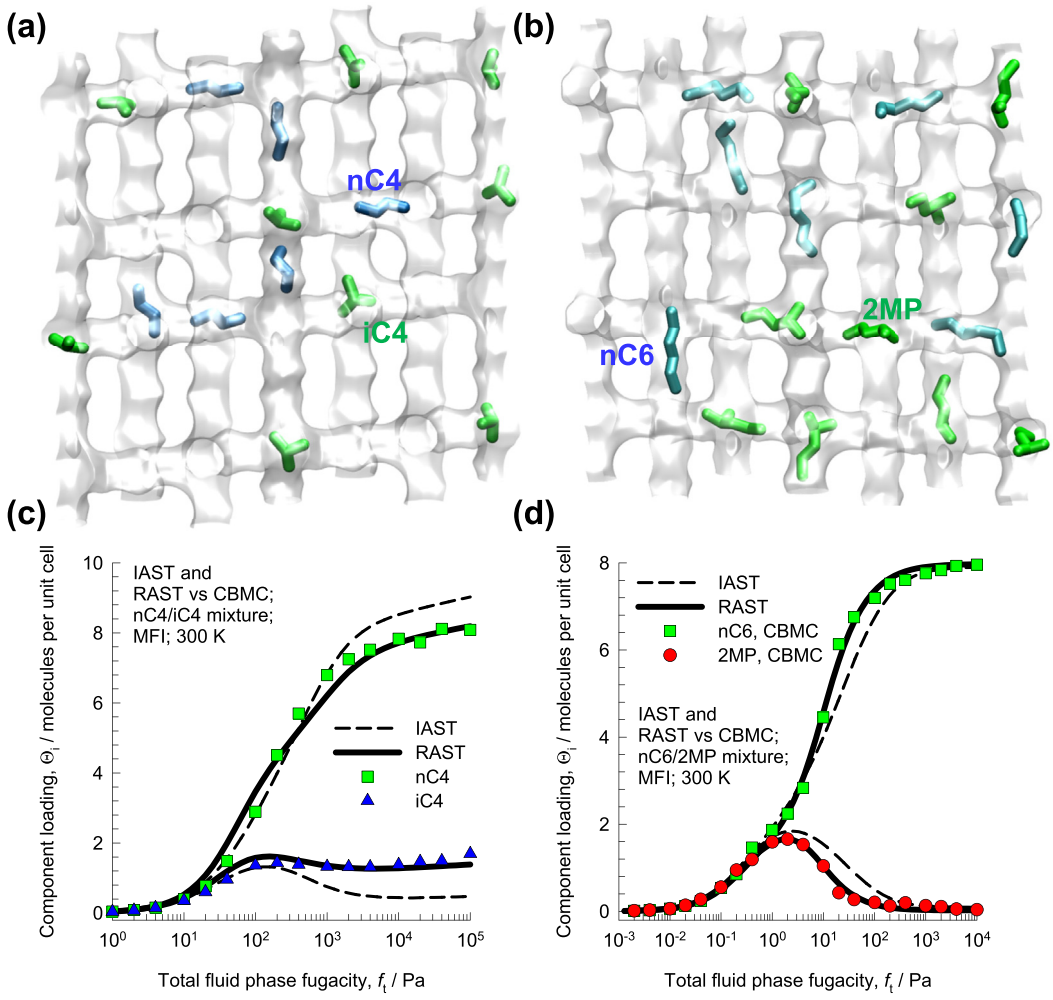

Fig. 19. (a, b) Computational snapshots showing the location of nC4, iC4, nC6, and 2 MP for (a) nC4/iC4, and (b) nC6/2 MP mixture adsorption within MFI zeolite at 300 K [76]. (c, d) CBMC simulations of loadings in the adsorbed phase in equilibrium with binary (c) nC4/iC4, and (d) nC6/2 MP mixtures with partial fugacities $f_1 = f_2$ in the bulk gas phase at 300 K. Also shown are the IAST (dashed lines), and RAST (continuous solid lines) estimations of component loadings. The isotherm fits, and Wilson parameters are provided in the Supplementary Material.

based on CBMC simulated data.

(1) The IAST estimates of component loadings, and selectivities are not in quantitative agreement with CBMC data under two fundamentally different scenarios: (a) formation of molecular clusters due to hydrogen bonding, and (c) inhomogeneous distribution of adsorbates due to preferential location and siting of one or more guest species.
(2) For modeling departures from the IAST estimates, activity coefficients need to be incorporated. For this purpose, the introduction of the correction factor $\left(1-\exp\left(-C\frac{\pi A}{RT}\right)\right)$ into the model describing the excess Gibbs free energy is essential in order to obtain the proper limiting behaviors for the activity coefficients γ_i. The Wilson model, used in this work, is found to provide reasonably good representation of thermodynamic non-idealities.
(3) For mixture separations in fixed bed adsorbers, there are often significant differences in the separation performance predicted by the IAST and RAST implementations. As illustrated by the breakthrough simulations in Figs. 9, 10 and 18, the IAST and RAST may anticipate opposite breakthrough sequences and selectivity reversals.
(4) For water/alcohol separations using zeolite membranes, thermodynamic non-idealities yield permeation selectivities that are significantly higher, by about an order of magnitude, that those estimated using the IAST. For proper design of membrane pervaporation processes, the use of the RAST is essential [45,60].
(5) For CO_2 capture applications, the preferential location at window regions, and within pockets, cause the IAST to overestimate the adsorption selectivities. Similarly, congregation of CO_2, H_2S, and alkenes around extra-framework cations cause failure of the IAST.
(6) For separations of linear and branched alkanes using MFI zeolite, non-ideality effects arise due to preferential location of the branched alkanes at the channel intersections that offer more "legroom".

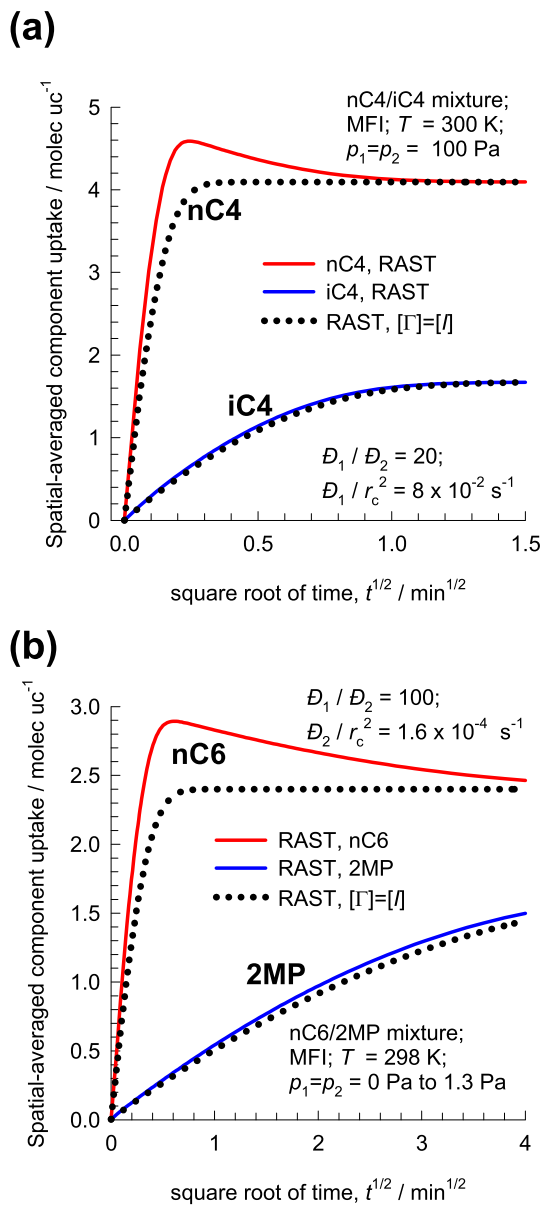

Fig. 20. Transient uptake of (a) nC4/iC4, and (b) nC6/2 MP mixture in MFI crystal at 300 K. The continuous solid lines are RAST calculations using the Maxwell-Stefan diffusion model that include thermodynamic coupling effects. The dotted lines are simulations in which the matrix of thermodynamic correction factors is taken to be the identity matrix $\begin{bmatrix} \Gamma_{11} & \Gamma_{12} \\ \Gamma_{21} & \Gamma_{22} \end{bmatrix} \rightarrow \begin{bmatrix} 1 & 0 \\ 0 & 1 \end{bmatrix}$. All data inputs and computational details are provided in the Supplementary Material.

Notation

A	surface area per kg of framework, $m^2\ kg^{-1}$
c_i	molar concentration of species i, mol m^{-3}
c_{i0}	molar concentration of species i in fluid mixture at inlet to adsorber, mol m^{-3}
C	constant used in equation (7), kg mol^{-1} or uc $molecule^{-1}$
$Đ_i$	M-S diffusivity of component i for molecule-pore interactions, $m^2\ s^{-1}$
f_i	partial fugacity of species i, Pa
f_t	total fugacity of bulk fluid mixture, Pa
$[I]$	Identity matrix with elements δ_{ij}, dimensionless
L	length of packed bed adsorber, m
n	number of species in the mixture, dimensionless
N_i	molar flux of species i defined in terms of the membrane area, mol $m^{-2}\ s^{-1}$
p_i	partial pressure of species i, Pa
p_t	total system pressure, Pa
P_i^0	sorption pressure, Pa
q_i	molar loading of species i, mol kg^{-1}
$q_{i,sat}$	molar loading of species i at saturation, mol kg^{-1}
q_t	total molar loading of mixture, mol kg^{-1}
R	gas constant, 8.314 J $mol^{-1}\ K^{-1}$
S_{ads}	adsorption selectivity, dimensionless
S_{perm}	permeation selectivity, dimensionless
t	time, s
T	absolute temperature, K
u	superficial gas velocity in packed bed, m s^{-1}
x_i	mole fraction of species i in adsorbed phase, dimensionless
y_i	mole fraction of species i in bulk fluid mixture, dimensionless

Greek letters

γ_i	activity coefficient of component i in adsorbed phase, dimensionless
Γ_{ij}	thermodynamic factors, dimensionless
$[\Gamma]$	matrix of thermodynamic factors, dimensionless
δ	thickness of membrane, m
δ_{ij}	Kronecker delta, dimensionless
ε	voidage of packed bed, dimensionless
Λ_{ij}	Wilson parameters, dimensionless
μ_i	molar chemical potential, J mol^{-1}
π	spreading pressure, N m^{-1}
ρ	framework density, kg m^{-3}
τ	time, dimensionless

Subscripts

0	upstream face of membrane
1	referring to species 1
2	referring to species 2
i,j	components in mixture
i	referring to component i
t	referring to total mixture
sat	referring to saturation conditions

Superscripts

0	referring to pure component loading
excess	referring to excess parameter

Appendix A. Supplementary data

Supplementary data related to this article can be found at http://dx.doi.org/10.1016/j.micromeso.2018.03.013.

References

[1] R.K. Motkuri, P.K. Thallapally, H.V.R. Annapureddy, L. Dang, R. Krishna, S.K. Nune, C.A. Fernandes, J. Liu, B.P. McGrail, Chem. Commun. 51 (2015) 8421–8424.
[2] J.J. Gutierrez-Sevillano, S. Calero, R. Krishna, J. Phys. Chem. C 119 (2015) 3658–3666.
[3] J.J. Gutierrez-Sevillano, S. Calero, R. Krishna, Phys. Chem. Chem. Phys. 17 (2015) 20114–20124.
[4] R. Krishna, Phys. Chem. Chem. Phys. 17 (2015) 39–59.
[5] K. Zhang, R.P. Lively, M.E. Dose, A.J. Brown, C. Zhang, J. Chung, S. Nair, W.J. Koros, R.R. Chance, Chem. Commun. 49 (2013) 3245–3247.
[6] J.C. Saint-Remi, T. Rémy, V. van Huskeren, S. van de Perre, T. Duerinck, M. Maes, D.E. De Vos, E. Gobechiya, C.E.A. Kirschhock, G.V. Baron, J.F.M. Denayer, ChemSusChem 4 (2011) 1074–1077.
[7] C.-T. He, L. Jiang, Z.-M. Ye, R. Krishna, Z.-S. Zhong, P.-Q. Liao, J. Xu, G. Ouyang, J.-P. Zhang, X.-M. Chen, J. Am. Chem. Soc. 137 (2015) 7217–7223.
[8] S. Van der Perre, T. Van Assche, B. Bozbiyik, J. Lannoeye, D.E. De Vos, G.V. Baron, J.F.M. Denayer, Langmuir 30 (2014) 8416–8424.
[9] A. Karmakar, A. Kumar, A.K. Chaudhari, P. Samantha, A.V. Desai, R. Krishna, S.K. Ghosh, Chem. Eur J. 22 (2016) 4931–4937.

[10] S. Mukherjee, B. Joarder, A.V. Desai, B. Manna, R. Krishna, S.K. Ghosh, Inorg. Chem. 54 (2015) 4403–4408.
[11] A. Torres-Knoop, R. Krishna, D. Dubbeldam, Angew. Chem. Int. Ed. 53 (2014) 7774–7778.
[12] D. Dubbeldam, R. Krishna, S. Calero, A.Ö. Yazaydın, Angew. Chem. Int. Ed. 51 (2012) 11867–11871.
[13] Z.R. Herm, B.M. Wiers, J.M. Van Baten, M.R. Hudson, P. Zajdel, C.M. Brown, N. Maschiocchi, R. Krishna, J.R. Long, Science 340 (2013) 960–964.
[14] R. Krishna, RSC Adv. 7 (2017) 35724–35737.
[15] R. Krishna, RSC Adv. 5 (2015) 52269–52295.
[16] R. Krishna, J.M. van Baten, Phys. Chem. Chem. Phys. 19 (2017) 20320–20337.
[17] R. Krishna, Separ. Purif. Technol. 194 (2018) 281–300 https://doi.org/10.1016/j.seppur.2017.11.056.
[18] R. Krishna, J.M. van Baten, Separ. Purif. Technol. 87 (2012) 120–126.
[19] D.M. Ruthven, Principles of Adsorption and Adsorption Processes, John Wiley, New York, 1984.
[20] A.L. Myers, J.M. Prausnitz, AIChE J. 11 (1965) 121–130.
[21] F.R. Siperstein, A.L. Myers, AIChE J. 47 (2001) 1141–1159.
[22] S. Sircar, Ind. Eng. Chem. Res. 45 (2006) 5435–5448.
[23] M. Konno, M. Teranayabashi, Y. Takako, S. Saato, J. Chem. Eng. Jpn. 18 (1985) 398–408.
[24] M. Sakuth, J. Meyer, J. Gmehling, J. Chem. Eng. Data 40 (1995) 895–899.
[25] M. Hefti, D. Marx, L. Joss, M. Mazzotti, Microporous Mesoporous Mater. 215 (2015) 215–228.
[26] R. Krishna, J.M. van Baten, J. Membr. Sci. 360 (2010) 323–333.
[27] F. Gholipour, M. Mofarahi, J. Supercrit. Fluids 111 (2016) 47–54.
[28] E. Costa, G. Calleja, A. Jimenez, J. Pau, J. Chem. Eng. Data 36 (1991) 218–224.
[29] S. Li, J.L. Falconer, R.D. Noble, R. Krishna, Ind. Eng. Chem. Res. 46 (2007) 3904–3911.
[30] S. Li, J.L. Falconer, R.D. Noble, R. Krishna, J. Phys. Chem. C 111 (2007) 5075–5082.
[31] M. Mofarahi, F. Gholipour, Microporous Mesoporous Mater. 200 (2014) 47–54.
[32] M.S. Shah, M. Tsapatsis, J.I. Siepmann, Chem. Rev. 117 (2017) 9755–9803.
[33] O. Talu, I. Zwiebel, AIChE J. 32 (1986) 1263–1276.
[34] G. Calleja, A. Jimenez, J. Pau, L. Domínguez, P. Pérez, Gas Separ. Purif. 8 (1994) 247–256.
[35] S.H. Hyun, R.P. Danner, J. Chem. Eng. Data 27 (1982) 196–200.
[36] G. Calleja, J. Pau, J.A. Calles, J. Chem. Eng. Data 43 (1998) 994–1003.
[37] M. Mofarahi, S.M. Salehi, Adsorption 19 (2013) 101–110.
[38] C.-W. Wu, S. Sircar, Separ. Purif. Technol. 170 (2016) 453–461.
[39] D. Frenkel, B. Smit, Understanding Molecular Simulations: from Algorithms to Applications, Academic Press, San Diego, 2002.
[40] B. Smit, R. Krishna, Chem. Eng. Sci. 58 (2003) 557–568.
[41] T.J.H. Vlugt, R. Krishna, B. Smit, J. Phys. Chem. B 103 (1999) 1102–1118.
[42] O. Talu, A.L. Myers, AIChE J. 34 (1988) 1887–1893.
[43] H. Zhang, S. Wang, Environ. Sci. Technol. 51 (2017) 5552–5562.
[44] S. Sochard, N. Fernandes, J.-M. Reneaume, AIChE J. 56 (2010) 3109–3119.
[45] N. Mittal, P. Bai, I. Siepmann, P. Daoutidis, M. Tsapatsis, J. Membr. Sci. 540 (2017) 464–476.
[46] R. Krishna, J.M. van Baten, Langmuir 26 (2010) 10854–10867.
[47] R. Krishna, J.M. van Baten, J. Membr. Sci. 360 (2010) 476–482.
[48] R. Krishna, J.M. van Baten, J. Phys. Chem. C 114 (2010) 13154–13156.
[49] R. Krishna, J.M. van Baten, Phys. Chem. Chem. Phys. 15 (2013) 7994–8016.
[50] R. Krishna, J.M. van Baten, Microporous Mesoporous Mater. 138 (2011) 228–234.
[51] R. Krishna, J.M. van Baten, Microporous Mesoporous Mater. 142 (2011) 745–748.
[52] J. Kärger, T. Binder, C. Chmelik, F. Hibbe, H. Krautscheid, R. Krishna, J. Weitkamp, Nat. Mater. 13 (2014) 333–343.
[53] J.Y. Wu, Q.L. Liu, Y. Xiong, A.M. Zhu, Y. Chen, J. Phys. Chem. B 113 (2009) 4267–4274.
[54] C. Zhang, X. Yang, Fluid Phase Equil. 231 (2005) 1–10.
[55] T.R.C. Van Assche, T. Duerinck, S. Van der Perre, G.V. Baron, J.F.M. Denayer, Langmuir 30 (2014) 7878–7883.
[56] T. Remy, J.C. Saint-Remi, R. Singh, P.A. Webley, G.V. Baron, J.F.M. Denayer, J. Phys. Chem. C 115 (2011) 8117–8125.
[57] Y. Hasegawa, C. Abe, M. Nishioka, K. Sato, T. Nagase, T. Hanaoka, J. Membr. Sci. 364 (2010) 318–324.
[58] Y. Hasegawa, H. Hotta, K. Sato, T. Nagase, F. Mizukami, J. Membr. Sci. 347 (2010) 193–196.
[59] J. Kuhn, J.M. Castillo-Sanchez, J. Gascon, S. Calero, D. Dubbeldam, T.J.H. Vlugt, F. Kapteijn, J. Gross, J. Phys. Chem. C 113 (2009) 14290–14301.
[60] M. Pera-Titus, C. Fité, V. Sebastián, E. Lorente, J. Llorens, F. Cunill, Ind. Eng. Chem. Res. 47 (2008) 3213–3224.
[61] X. Shu, X. Wang, Q. Kong, X. Gu, N. Xu, Ind. Eng. Chem. Res. 51 (2012) 12073–12080.
[62] R. Krishna, J.M. van Baten, Separ. Purif. Technol. 76 (2011) 325–330.
[63] P. Bai, M. Tsapatsis, I.J. Siepmann, Langmuir 28 (2012) 15566–15576.
[64] A. Nalaparaju, X.S. Zhao, J.W. Jiang, J. Phys. Chem. C 114 (2010) 11542–11550.
[65] R. Krishna, Microporous Mesoporous Mater. 185 (2014) 30–50.
[66] R. Krishna, J. Membr. Sci. 540 (2017) 261–276.
[67] R. Krishna, Phys. Chem. Chem. Phys. 18 (2016) 15482–15495.
[68] R. Krishna, J.M. van Baten, Phys. Chem. Chem. Phys. 13 (2011) 10593–10616.
[69] R. Krishna, J.M. van Baten, Microporous Mesoporous Mater. 137 (2011) 83–91.
[70] R. Krishna, J.M. van Baten, Microporous Mesoporous Mater. 258 (2018) 151–169 https://doi.org/10.1016/j.micromeso.2017.09.014.
[71] R. Krishna, J.M. van Baten, Separ. Purif. Technol. 61 (2008) 414–423.
[72] H. Wu, J.M. Simmons, G. Srinivas, W. Zhou, T. Yildrim, J. Phys. Chem. Lett. 1 (2010) 1946–1951.
[73] E.D. Bloch, W.L. Queen, R. Krishna, J.M. Zadrozny, C.M. Brown, J.R. Long, Science 335 (2012) 1606–1610.
[74] S. Chavan, F. Bonino, L. Valenzano, B. Civalleri, C. Lamberti, N. Acerbi, J.H. Cavka, M. Leistner, S. Bordiga, J. Phys. Chem. C 117 (2013) 15615–15622.
[75] R. Krishna, J.M. van Baten, Chem. Eng. J. 140 (2008) 614–620.
[76] T. Titze, C. Chmelik, J. Kärger, J.M. van Baten, R. Krishna, J. Phys. Chem. C 118 (2014) 2660–2665.
[77] R. Krishna, D. Paschek, Phys. Chem. Chem. Phys. 3 (2001) 453–462.
[78] M. Fernandez, J. Kärger, D. Freude, A. Pampel, J.M. van Baten, R. Krishna, Microporous Mesoporous Mater. 105 (2007) 124–131.
[79] R. Krishna, J.M. van Baten, Chem. Eng. Sci. 63 (2008) 3120–3140.
[80] R. Krishna, J.M. van Baten, Langmuir 26 (2010) 3981–3992.